Analysis of Oblique Shock Waves Over a Supersonic Aircraft Nose with Emphasis on Stagnation Pressure and Entropy Change

a project presented to
The Faculty of the Department of Aerospace Engineering
San Jose State University

in partial fulfillment of the requirement for the degree
Masters of Science in Aerospace Engineering

by

Majd A Alhakim

December 2025



approved by
Dr. Yawo Ezunkpe
Faculty Advisor

© 2025
Majd A. Alhakim
All Rights Reserved
San José, California

Abstract

Analysis of Oblique Shock Waves Over a Supersonic Aircraft Nose with Emphasis on Stagnation Pressure and Entropy Change

Majd A Alhakim

In supersonic flow, the shape of the nose impacts how shocks arise, how intense they are, and how much quality of the flow is lost as the air turns around the aircraft. A blunt or poorly constructed nose produces significant shocks that generate big jumps in pressure, temperature, and entropy, resulting in higher overall pressure losses, increased drag, and less efficient flow entering the remainder of the aircraft. By carefully constructing the nose geometry, such as applying a multi-wedge (double-wedge) layout that can divide a big flow deflection into smaller stages, resulting in lesser oblique shocks rather than a single strong one. This study presents a straightforward, universal approach, combining basic CFD based shape tuning at important Mach values. This reduces total pressure loss across the shocks and limits entropy generation, how different nose geometries at Mach 2 affect the shock pattern, downstream flow (Mach, pressure, temperature, density, velocity), and overall thermodynamic efficiency. Understanding the relationship between nose shape and shock behavior is critical for analyzing the CFD results and comparing them to theoretical oblique shock predictions. Engineers make early, data driven decisions that increase range, reduce fuel consumption, and protect the airframe by making quick shape adjustments.

Acknowledgements

I'd like to thank my project advisor, Dr. Yawo Ezunkpe, for his guidance and support during the course of this research project. His suggestions and support had a major impact on the direction and quality of my research.

I'd also like to thank Dr. Nikos Mourtos, department head at San José State University, for his continued support and commitment to student success. His leadership and vision have helped to create an environment in which projects like this can succeed.

A special thanks to my parents, for your constant faith in me and the principles you created for me, which have carried me through this journey.

And to my wife, May, your love, patience, and encouragement have served as my rock throughout this process. I am very grateful.

Table of Contents

Abstract....i
Acknowledgements....ii
Table of Contents....iii
List of Figures....v
List of Tables....vi
1 Introduction....7
1.1 Motivation....7
1.2 Literature Review....7
1.2.1 Overview....7
1.2.2 Supersonic Oblique Shock Theory and Total Pressure Loss....8
1.2.2.1 Normal and Oblique Shock Relation....8
1.2.2.2 Stagnation Pressure, Entropy, and Shock Strength....9
1.2.3 Single Wedge Supersonic Flows....10
1.2.3.1 Numerical Modeling of a Single Wedge....10
1.2.3.2 Theory and CFD analysis for Property Jumps and Shock Angle....11
1.2.4 Double Wedge Geometries and Shock-Shock Interactions....11
1.2.4.1 Turbulent Double Wedge Flow and Aft-Wedge Angle Effects....11
1.2.4.2 Experimental Studies on Double-Wedge Type-V Shock-Shock Interactions 12
1.2.4.3 Hypersonic Shock-Shock Interactions over Wedges....14
1.2.5 Nose Geometry and Supersonic External Flows....15
1.2.5.1 CFD Studies of Varying Nose Profiles....15
1.2.5.2 Relevance of Nose shape to Shock Formation and Flow Quality....15
1.2.6 Supersonic Inlets and Forebody Shock Systems....16
1.2.6.1 External Compression Inlets at Mach 1.4 to 2.1....16
1.2.6.2 Variable Geometry Inlets and CFD Based Optimization....17
1.2.7 High Speed Wedge Flows and Detonation....17
1.2.7.1 Wedge Stabilized Oblique Detonation Waves....17
1.3 Project Proposal....18
1.4 Methodology....19
2 F-16 Fighting Falcon....21
2.1 Chapter Summary....21
2.2 F-16 Fighting Falcon Brief History....21
3 Theoretical Results....23
3.1 Chapter Overview....23
3.2 Theoretical Upstream Values Calculations....23
3.2.1 Theoretical Calculations for Wedge at 15^{o}....26

3.2.2 Theoretical Calculations for Double Wedge at 7.64° and 14.2°.....30
3.3 Entropy Change and Stagnation Pressure Ratio of Both Wedges.....34
4 Experimental Results.....36
4.1 Chapter Overview.....36
4.2 Geometry.....36
4.3 Mesh Setup.....37
4.4 CFD Setup.....38
4.4.1 Experimental Results for 15° Wedge.....39
4.4.2 Experimental results for 7.64° and 14.28° double wedge.....48
4.5 Entropy Change and Stagnation Pressure Ratio of Experimental Wedges.....57
5 Entropy and Stagnation Pressure: Theoretical vs Experimental Percent Error.....59
5.1 Overview.....59
5.2 Percent Error and Comparisons.....59
6 Comprehensive Discussion.....61
7 Conclusion and Future Work.....62
References.....63
Appendix A: Matlab Script for Theoretical Oblique Shock over a Supersonic Aircraft Nose (1 Wedge).....65
Appendix B: Matlab Script for Theoretical Oblique Shock over a Supersonic Aircraft Nose Double Wedge (2 Wedge).....69

List of Figures

Figure 1.1 Properties of a normal shock wave as a function of upstream Mach number [6]..... 11
Figure 1.2 Contour and convergence plot of pressure and density [1]..... 12
Figure 1.3 Two dimensional geometry of Swantek and Austin's double-wedge [2]..... 14
Figure 1.4 Mean Schlieren and RMS visualization from three second wedge angles [3]..... 15
Figure 1.5 Edney catalogued shock interaction types [9]..... 16
Figure 1.6 Mach number contours for Mach 1.7 and Mach 2.0 inlets at subcritical and supercritical operating conditions [4]..... 18
Figure 1.7 A viscous double-angle wedge in a Mach = 5, and T = 700 K flow. The subsonic region is enclosed by a dashed line. [5]..... 20
Figure 2.1 F-16 Dimension layout and equipment placement [19]..... 24
Figure 3.1 Values for specific heat ratio (γ) and gas constant (R) [11]..... 26
Figure 3.2 Earth atmosphere model [10]..... 27
Figure 3.3 Mach number ratio [12]..... 27
Figure 3.4 Oblique shock wave flow at 15^{o} wedge..... 29
Figure 3.5 Matlab graphs of flow properties across shock at 15^{o} (theoretical)..... 32
Figure 3.6 Oblique shock wave flow of double wedge at 7.64^{o} and 14.2^{o}..... 33
Figure 3.7 Matlab graphs of flow properties across shocks at 7.64^{o} and 14.2^{o} (theoretical)..... 36
Figure 4.1 Sketch of single and double wedge on ANSYS design modeler..... 39
Figure 4.2 Mesh and named selections of single wedge and double wedge..... 40
Figure 4.3 Residuals plot (single wedge)..... 41
Figure 4.4 Static pressure and dynamic pressure plots (single wedge)..... 42
Figure 4.5 Static temperature and density plots (single wedge)..... 44
Figure 4.6 Velocity magnitude and Mach plots (single wedge)..... 45
Figure 4.7 Static pressure and dynamic pressure contours (single wedge)..... 46
Figure 4.8 Static temperature and density contours (single wedge)..... 47
Figure 4.9 Velocity magnitude and Mach number contours (single wedge)..... 48
Figure 4.10 Residuals plot (double wedge)..... 50
Figure 4.11 Static pressure and dynamic pressure plots (double wedge)..... 51
Figure 4.12 Static temperature and density plots (double wedge)..... 53
Figure 4.13 Velocity magnitude and Mach plots (double wedge)..... 54
Figure 4.14 Static pressure and dynamic pressure contours (double wedge)..... 55
Figure 4.15 Static temperature and density contours (double wedge)..... 56
Figure 4.16 Velocity magnitude and Mach contours (double wedge)..... 57

List of Tables

Table 3.1 Upstream values specifications before shock..... 28
Table 3.2 Theoretical downstream values after shock at 15°..... 31
Table 3.3 Theoretical downstream values after shock at 7.64°..... 34
Table 3.4 Theoretical downstream values after shock at 14.28°..... 34
Table 3.5 Comparison of theoretical total stagnation pressure and entropy in single and double wedge configurations..... 37
Table 4.1 Experimental downstream values after shock at 15°..... 45
Table 4.2 Experimental downstream values after shock at 7.64°..... 50
Table 4.3 Experimental downstream values after shock at 14.28°..... 50
Table 4.4 Comparison of experimental total stagnation pressure and entropy in the single and double wedge configurations..... 52
Table 5.1 Theoretical vs experimental percent error..... 53

1 Introduction

1.1 Motivation

Supersonic aircraft operating around Mach 2 produce powerful oblique shocks at the nose, which control how the flow is turned, compressed, and thermodynamically degraded before it reaches the body of the airframe. Recent numerical work on single wedges at Mach 2 has demonstrated that even small compression ramps can cause significant changes in Mach number, pressure, and temperature, and that a careful comparison of theory and CFD is required to explain these changes in detail [1].

At the same time, research on double-wedge geometries shows that splitting the total flow deflection into two separate phases introduces new phenomena such as shock-shock interaction and shock-boundary-layer interaction, which can increase local loads and heat transfer while changing the overall compression pattern [2,3]. These findings imply that nose geometry is more than just a geometric option, it has a direct impact on how much total pressure is lost and how much entropy is generated as the flow goes through one or more shocks.

Total pressure recovery at the nose in a Mach 2 transport or fighter-class configuration is closely related to inlet performance, engine reliability, and overall propulsive efficiency, because any irreversible losses in the forebody shock system reduce the usable stagnation pressure available to a downstream inlet [4].

Research in high-speed reacting and non-reacting wedge flows has confirmed that total pressure loss across oblique shocks is a useful quantitative measure of shock strength, and that geometry-driven changes in shock structure can be directly interpreted as changes in stagnation pressure and entropy [5].

Building on these concepts, this report focuses on a clean, controlled comparison between a single-wedge and a double-wedge nose at Mach 2. It uses CFD and theoretical oblique shock relations to quantify changes in Mach number, pressure, temperature, density, and velocity across each shock. The objective is to evaluate total pressure loss and associated entropy increase for each nose design, and determine which geometry is more thermodynamically efficient in terms of weaker shocks and higher stagnation-pressure preservation.

1.2 Literature Review

1.2.1 Overview

In compressible-flow theory, the ideal benchmark for any supersonic compression system is isentropic turning with no loss of total (stagnation) pressure. Oblique shocks are naturally measured by how much they vary from this loss-free, no-entropy-change limit [6]. Canonical single-wedge designs offer a simple technique to investigate that deviation. Theory and CFD can be directly compared to quantify how a single oblique shock at a particular deflection angle and Mach number affects Mach, pressure, temperature, density, velocity, and stagnation pressure [1]. Double-wedge geometries build on this idea by adding a second compression corner and a second shock, resulting in more complicated shock systems whose strength and interaction patterns are highly influenced by the aft-wedge angle [2, 3]. At the same time, studies of

external-compression and variable-geometry inlets show that the design of the forebody shock system is primarily evaluated using total-pressure recovery, which links the structure and strength of shocks ahead of the inlet to engine operability and overall efficiency [4, 7]. Within this context, the current project employs a single-wedge nose as a baseline and a double-wedge nose as a modified geometry at Mach 2 to quantify how each configuration deviates from the ideal no-loss case, as well as to determine which nose more effectively preserves total pressure and minimizes entropy generation by comparing stagnation-pressure ratios and property jumps across shocks.

1.2.2 Supersonic Oblique Shock Theory and Total Pressure Loss

1.2.2.1 Normal and Oblique Shock Relation

Normal and oblique shock relations form the foundation for predicting how Mach number, pressure, temperature, and density change when a supersonic flow is compressed by a shock. Across a normal shock, which is perpendicular to the flow, static pressure, temperature, and density all rise while the Mach number falls to a lower (usually subsonic) value, these trends are summarized in Anderson's normal-shock relations, as well as the curves of $P2/P1$, $T2/T1$, $\rho 2/\rho 1$, and $M2$ vs. $M1$ all shown in Figure 1.1. Oblique shocks are similar to normal shocks in that they affect the velocity component that is normal to the shock surface. When a supersonic stream is turned into itself over a wedge or compression corner, a straight shock stands at an angle β to the incoming flow and deflects the flow at an angle θ. The normal component of Mach number determines the downstream state, while the deflection angle, shock angle, and upstream Mach number are linked using the standard θ-β-M relations [6].

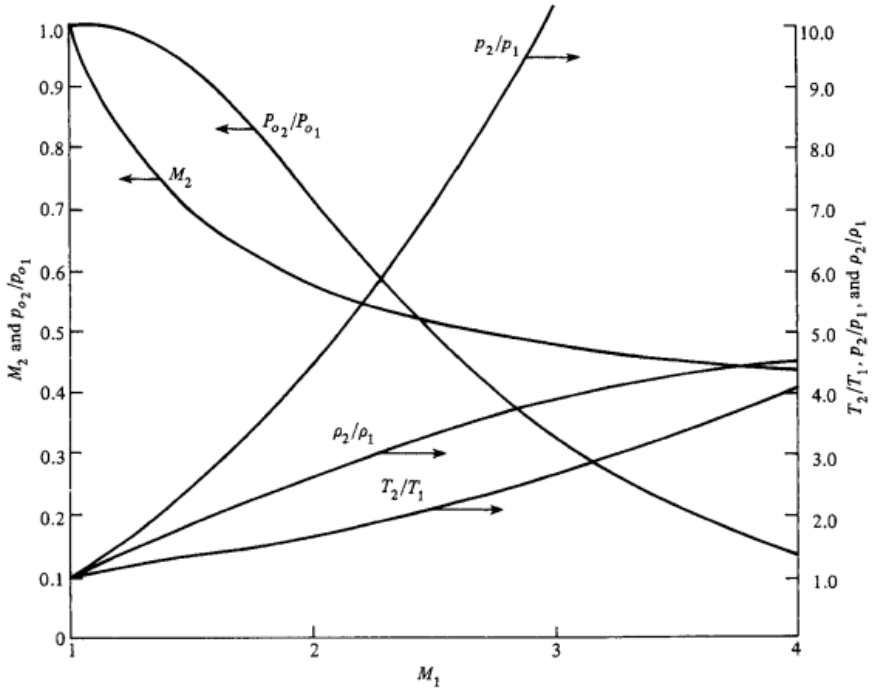


Figure 1.1 Properties of a normal shock wave as a function of upstream Mach number [6]

This project's single-wedge and double-wedge configurations closely match the sketches of wedges and cones with coupled oblique shocks, as well as the related θ-β-M diagrams. These relationships are used to calculate region-by-region changes in Regions 1-2-3 at Mach 2 and establish a theoretical baseline for how each wedge geometry affects flow along the nose.

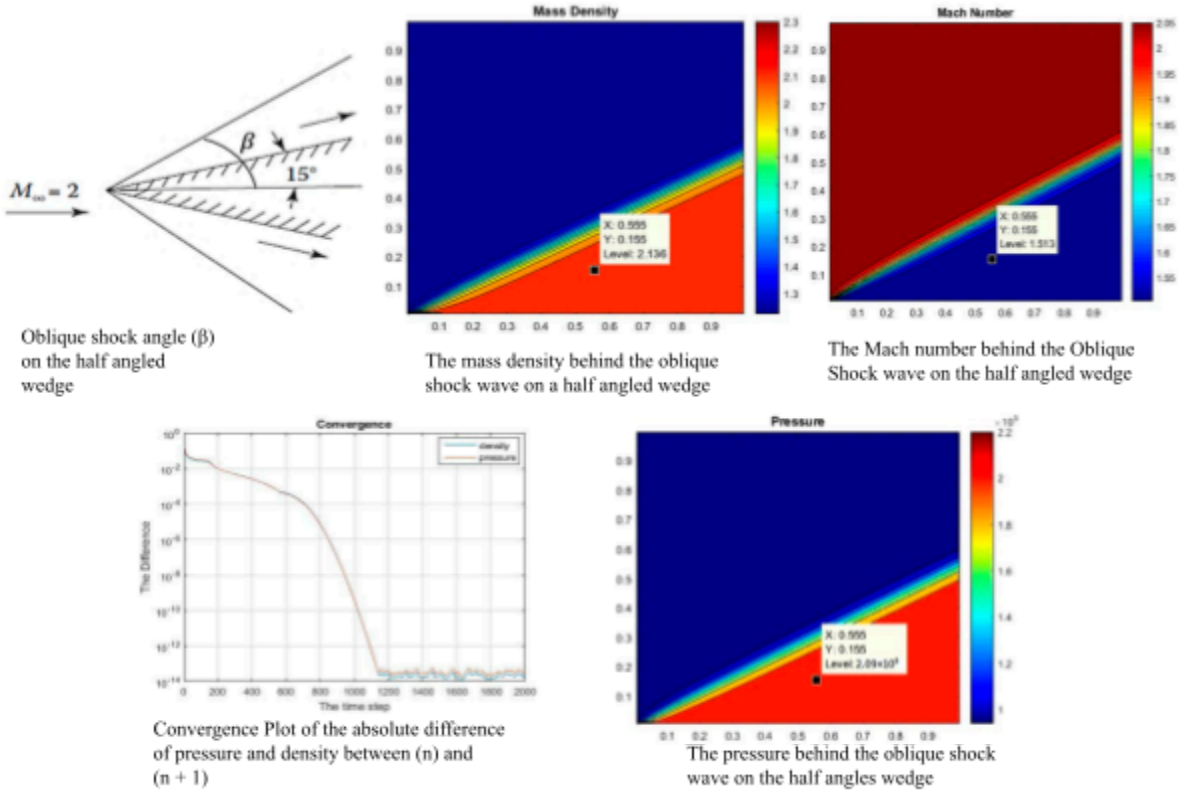
1.2.2.2 Stagnation Pressure, Entropy, and Shock Strength

In addition to static property jumps, shock relations also describe how total (stagnation) quantities and entropy change across a shock, which is critical for estimating aerodynamic and thermodynamic losses. For a stationary normal shock in a calorically perfect gas, the total temperature and enthalpy remain constant, while the total pressure drops as entropy increases. This tendency is frequently demonstrated by introducing hypothetical stagnation states upstream and downstream of the shock and showing that the ratio P02/P01 drops linearly with increasing upstream Mach number. The decrease in stagnation pressure therefore offers a direct quantitative indicator of irreversibility and shock strength [6]. In the current work, these ideas are used to establish metrics like P02/P01 for the first shock and P03/P01 for the cumulative effect of two shocks. By comparing these stagnation-pressure ratios and the entropy increase for single and double wedge noses at Mach 2, the analysis determines how far each configuration deviates from the ideal isentropic case and which geometry better preserves total pressure through the nose shock system.

1.2.3 Single Wedge Supersonic Flows

1.2.3.1 Numerical Modeling of a Single Wedge

Previous numerical work approximated supersonic flow across a basic two-dimensional wedge using the inviscid Euler equations and a finite volume approach that splits flux vectors. In that investigation, a Mach 2.0 freestream was guided over a 15° half-angle wedge, and the governing equations were solved on a structured grid until a consistent solution was obtained. The numerical results included the associated oblique shock created at the wedge leading edge, as well as the downstream distributions of pressure, density, temperature, and Mach number in the shock layer. The study also compared the calculated shock angle and post-shock parameters to traditional oblique-shock theory and found reasonable results, suggesting that a relatively simple Euler-based CFD model can consistently forecast the fundamental features of single-wedge supersonic flows at low computing cost [1].



Oblique shock angle (β) on the half angled wedge

The mass density behind the oblique shock wave on a half angled wedge

The Mach number behind the Oblique Shock wave on the half angled wedge

Convergence Plot of the absolute difference of pressure and density between (n) and (n + 1)

The pressure behind the oblique shock wave on the half angles wedge

Figure 1.2 Contour and convergence plot of pressure and density [1]

The contour plots in Figure 1.2 shows several viewpoints of Mach 2 flow striking a 15° wedge and producing an oblique shock. The mass-density contour shows a quick increase in air density over the slanted shock line, followed by a nearly equal distribution along the wedge surface. The Mach number contours demonstrate that the freestream starts at Mach 2, dips to

around Mach 1.5 after traversing the shock, and then stays almost constant, emphasizing the shock angle. The pressure contour follows the same pattern as static pressure, low and uniform upstream, with a sudden jump across the shock and a fairly constant value downstream along the wedge. The convergence validates the numerical solution's reliability, since the discrepancies in density and pressure between time steps decrease by many orders of magnitude before leveling out, showing that the solver has found a steady, stable solution for the flow field [1].

1.2.3.2 Theory and CFD analysis for Property Jumps and Shock Angle

Classical compressible-flow theory provides closed-form formulas for oblique shocks, relating the upstream Mach number and wedge deflection angle to the shock angle, as well as pressure, density, temperature, and Mach number jumps across the shock. The θ-β-M diagram and normal-shock equations apply to the normal component of entering flow, showing that increasing wedge angle or freestream Mach number strengthens shock and increases associated property jumps. These formulas were tested using numerical simulations of a Mach 2.0 flow over a 15^{o} wedge, which involved directly comparing the computed shock angle and downstream properties to theoretical predictions along the wedge surface [6]. The pressure and temperature rise across the leading-edge shock for this kind of single-wedge configuration is accurately described by the standard oblique-shock relations, according to the CFD results, which were found to match the theory within slight variations. This gives a good foundation that the same method can be used to interpret the single-wedge results of the current study [1, 6].

1.2.4 Double Wedge Geometries and Shock-Shock Interactions

1.2.4.1 Turbulent Double Wedge Flow and Aft-Wedge Angle Effects

Unsteady Reynolds-averaged Navier-Stokes simulations were used to analyze supersonic flow over double-wedge geometries in order to better understand how turbulence and aft-wedge angle affect shock interaction patterns. Mach 5 flow over a two-dimensional double wedge was examined using several turbulence models, and the numerical predictions were compared to known experimental behavior to determine which models accurately describe separation, reattachment, and heat-flux trends.The laminar assumption failed once strong contacts occurred, but turbulence models handled the separation zone and accompanying heating more accurately. Varying the aft-wedge angle between 45^{o} and 60^{o} resulted in noticeable variations in shock structure, including a shift from weaker interactions to configurations that generate Mach reflection and higher heating on the aft surface. These results demonstrate that the aft-wedge deflection angle has a significant impact on the intensity and distribution of stresses generated by double-wedge shock interactions at hypersonic speeds [2].

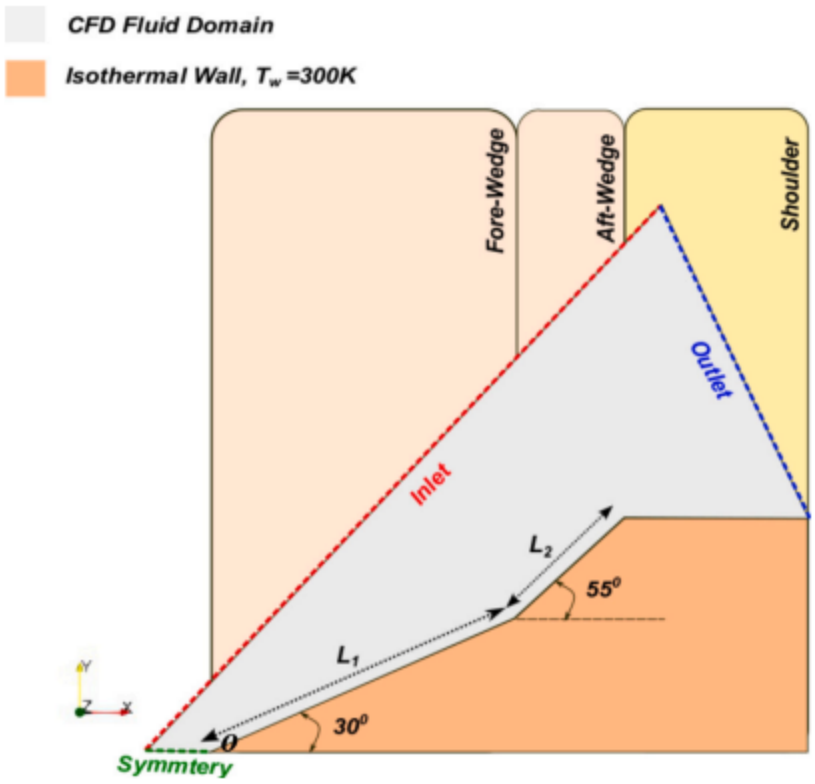


Figure 1.3 Two dimensional geometry of Swantek and Austin's double-wedge [2]

Figure 1.3 provides an annotated schematic of Swantek and Austin's double-wedge shape. In the study values of L1 and L2 are given, where L1 = 50.8 mm and L1−L2 = 0.5. For clarity, the wedge surface in pale orange and shoulder shown in pale yellow are color-coded. The flow direction is from left to right. The letter 'O' represents the origin [2].

1.2.4.2 Experimental Studies on Double-Wedge Type-V Shock-Shock Interactions

High-speed schlieren imaging and surface measurements have been used to study the unstable behavior of type-V shock-shock interactions on double-wedge surfaces. Mach 6.13 flow was driven across a double wedge with second-wedge angles of 45°, 55°, and 60°, resulting in noticeable changes in separation size and contact strength. Mean schlieren fields showed that raising the aft angle expanded the separation zone and exacerbated the interaction region, resulting in increased average pressure on the aft wedge. Root-mean-square schlieren visualization, along with correct orthogonal decomposition and spectral analysis, revealed discrete low- and high-frequency motions associated with large-scale shock displacement and smaller-scale downstream fluctuations. These findings suggest that type-V interactions are fundamentally unstable, involve many coupled spatial structures, and are sensitive to geometrical changes in the double-wedge arrangement [3].

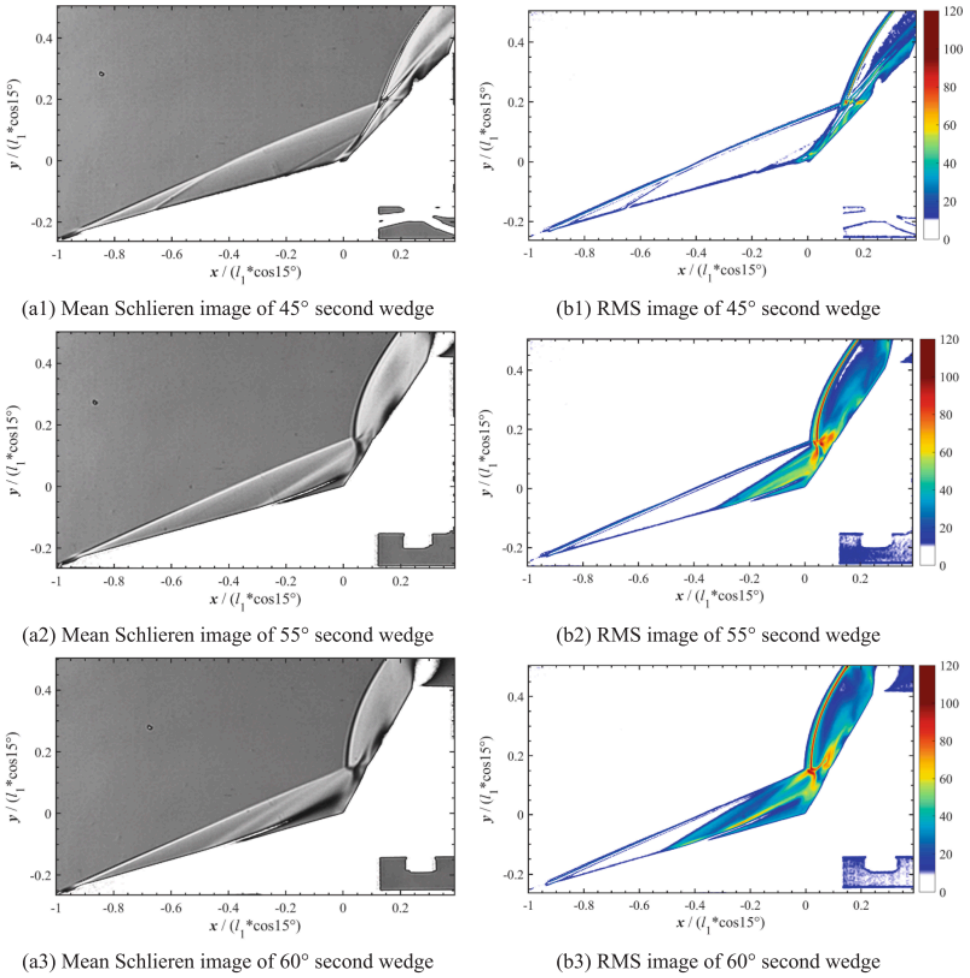


Figure 1.4 Mean Schlieren and RMS visualization from three second wedge angles [3]

Figure 1.4 compares the flow across a double wedge with second-wedge angles of 45°, 55°, and 60° at Mach 6.13. The left column contains mean Schlieren representation, which are time-averaged views of the flow's density gradients. In each example, a type-V shock/shock interaction occurs when the shock from the first wedge meets the bow shock from the second wedge. As the second-wedge angle rises from 45° to 60°, the separation bubble between the two wedges becomes longer and thicker, the bow shock rises further from the surface, and the entire shock system becomes stronger and more curved. This clearly verifies that a greater second-wedge angle results in a larger separated region and a stronger interaction zone [3].

The right column displays the comparable RMS (root-mean-square) Schlieren images, which show where the flow is most unstable. Brighter colors indicate locations with large density changes, which are centered in the shock-shock interaction zone and surrounding the separation bubble. Moving from 45° to 60°, the high-RMS zones expand and worsen, showing that the shock system and separated flow become increasingly unstable as the second-wedge angle grows. This is closely related to the study's result that increasing the second-wedge angle increases both the size of the separation zone and the strength of unsteadiness, as does the average pressure on the second-wedge wall [3].

1.2.4.3 Hypersonic Shock-Shock Interactions over Wedges

Shock-shock interactions caused by wedge-produced shocks at hypersonic speeds were investigated utilizing surface heating measurements and flow visualization. A planar oblique shock from a narrow wedge was applied to the bow shock of a cylindrical or fin-type leading edge, resulting in interaction patterns consistent with Edney's classification. Phosphor-thermography data provided detailed surface temperature fields, which were then processed using one- and two-dimensional heat-conduction models to calculate local heating rates. The interaction zones produced acute, localized heat transfer peaks, the amplitude of which was highly determined by the distance between the geometry and alignment of the intersecting shocks. Two-dimensional conduction analysis produced greater peak values than one-dimensional reductions, highlighting the significance of lateral heat spreading in places with steep gradients caused by shock-shock impingement [9].

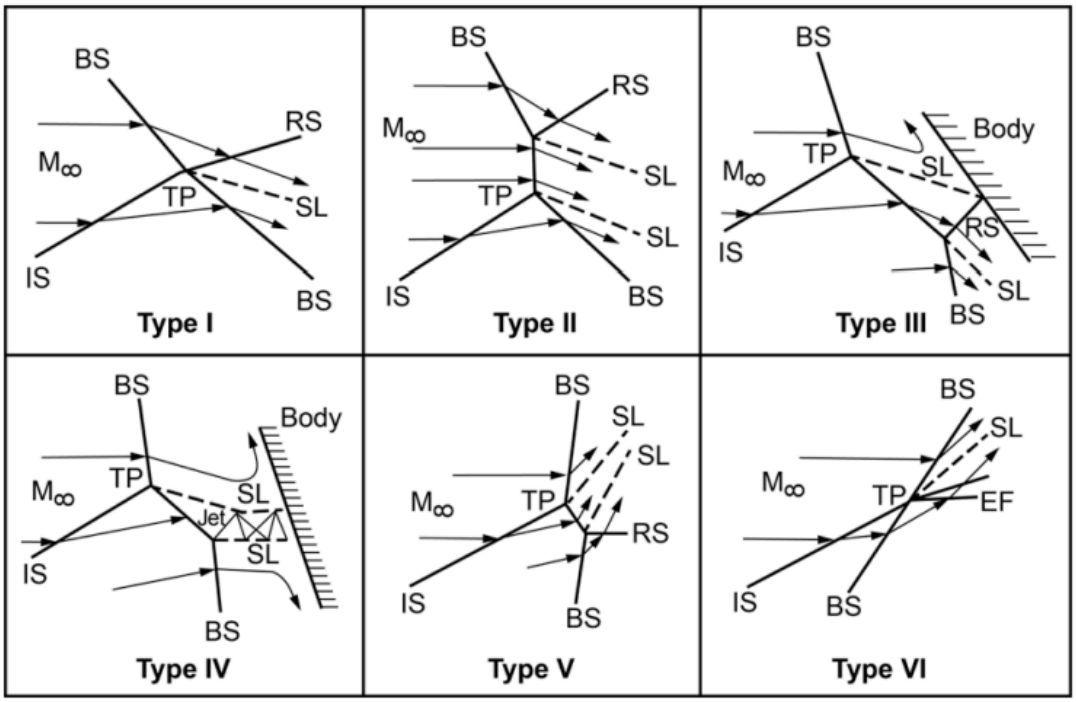


Figure 1.5 Edney catalogued shock interaction types [9]

Figure 1.5 shows the Edney Types, a series of shock-shock interaction patterns. These shock types illustrate the various ways in which two shock waves might collide, combine, reflect, or form complex structures in supersonic and hypersonic flow. The image gives a visual foundation for understanding why certain interactions result in higher heating or pressure loads than others.

In simple terms, each box in the diagram shows a possible "interaction mode" that can occur when an incident shock (IS) meets a bow shock (BS) from a body such as a wedge, fin, or leading edge. Depending on the angles, shock strengths, and geometry, the interaction can

produce a reflected shock (RS), a triple point (TP) where many shock structures meet, and one or more shear layers (SL) [9].

Types I-III show increasingly complex shock crossings. In these situations, the two shocks simply collide and create a reflected shock and shear layer. These types emerge when shocks collide without forming a jet or a separate flow zone [9].

Type IV is one of the most serious interactions. It has a jet-like structure that forms between the shocks and may significantly increase surface heating on surrounding bodies. This type is particularly significant in hypersonic vehicle design due to the possibility of damaging thermal loads [9].

Type V has several shear layers and is the result of a very powerful intersection of shocks. This kind is associated with a significant degree of flow instability [9].

Type VI has an expansion fan (EF) that occurs after the triple point, demonstrating how the shock connection can weaken or open up depending on the shape [9].

1.2.5 Nose Geometry and Supersonic External Flows

1.2.5.1 CFD Studies of Varying Nose Profiles

Computational analyses of several axisymmetric nose profiles have been used to investigate how shape affects aerodynamic behavior under subsonic and transonic situations. Several practical nose geometries were modeled in ANSYS, and the surface pressure coefficient distributions at Mach 0.8 were analyzed to determine which shapes delay the development of local supersonic pockets and normal shocks. The simulations aimed to bring the pressure coefficient values closer to ambient pressure, which increased the critical Mach number and reduced unfavorable pressure gradients over the forebody.Some more gradual nose profiles result in better pressure recovery and less gradients along the cylindrical afterbody, which helps to delay boundary-layer separation and vortex generation. These results provide a CFD-based basis for selecting nose shapes that offer improvements in pressure characteristics and higher usable Mach values for slim bodies and missiles [8].

1.2.5.2 Relevance of Nose shape to Shock Formation and Flow Quality

Nose geometry has a direct impact on how shocks arise and how smoothly external flow develops throughout the body of the car. Classical compressible-flow theory demonstrates that for a given Mach number, sharper deflection angles generate bigger oblique or even normal shocks with higher jumps in pressure, temperature, and entropy, while more gradual forms generate weaker shocks and smaller property changes [6]. The CFD comparison of nose profiles supports this behavior by indicating that forms that increase the base-of-forebody pressure minimize the adverse pressure gradient over the cylindrical body, minimizing separation and large-scale vortex generation downstream. When the local supersonic region ends in a powerful shock near the nose, the resulting pressure jump can cause early separation and unsteady forces on the tail surfaces, when the nose shape spreads the compression over a longer distance, the flow remains more connected and consistent. The theoretical relations for shock strength and the numerical results for pressure gradients show that nose shape is a significant design variable for regulating shock location, lowering drag, and maintaining superior flow quality over the rest of the airframe [6, 8].

1.2.6 Supersonic Inlets and Forebody Shock Systems

1.2.6.1 External Compression Inlets at Mach 1.4 to 2.1

External compression inlets use a sequence of oblique shocks generated ahead of the cowl to slow and compress the freestream flow before it enters the engine. Computational studies of axisymmetric inlets built for freestream circumstances ranging from Mach 1.4 to 2.0 have demonstrated how off-design variations, such as changes in engine mass flow, angle of attack, and ambient Mach number, affect inlet performance. Flow distortion, total pressure recovery, and cowl wave drag were tested under a variety of operating conditions, and the results showed that even small variations from the design Mach number can shift shock positions, change the strength of compression waves, and alter the effectiveness of bleed systems. The analyses also showed how certain designs maintain more robust shock structures under off-design situations, resulting in improved pressure recovery and less deformation at the engine face. These results give a mathematical basis for selecting intake layouts that can endure mission-profile fluctuations while meeting aerodynamic and propulsion requirements [4].

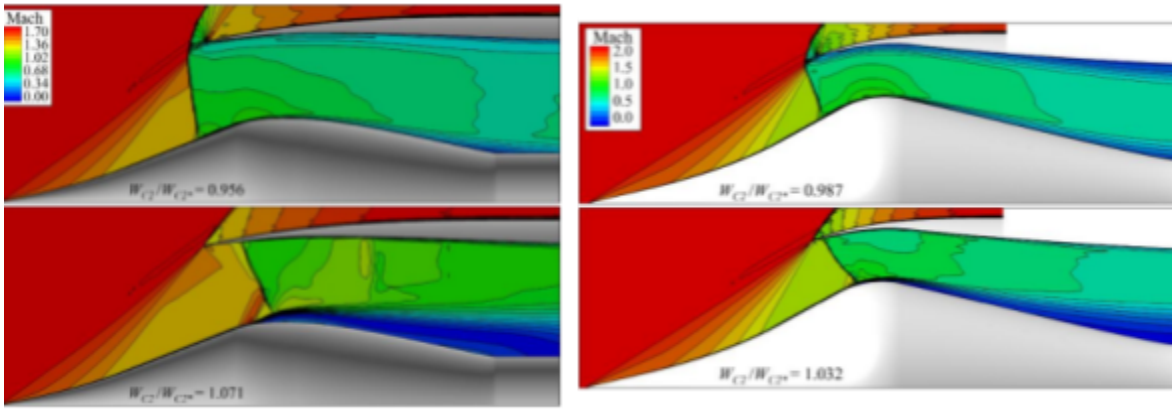


Figure 1.6 Mach number contours for Mach 1.7 and Mach 2.0 inlets at subcritical and supercritical operating conditions [4]

Figure 1.6 depicts how the flow inside the axisymmetric spike inlet varies from subcritical to supercritical operating conditions at cruise for Mach 1.7 and Mach 2.0. In each pair, the contour on the left is the most subcritical, the engine is swallowing less than the collected flow, which means the terminal normal shock rests just outside the cowl lip, which allows part of the slowed, subsonic air to escape. The Mach contours show a shorter subsonic region in the intake and a somewhat smooth deceleration of the incoming Mach 1.7 or Mach 2.0 flow [4].

In the right contour of each pair, the inlet is supercritical, the engine requires greater flow, therefore the terminal shock is drawn within the inlet. The contours reveal a greater region of low-Mach shown in blue/green flow within the duct, as well as a stronger internal shock system, resulting in increased total-pressure loss and distortion at the engine face. Together, these visuals show how going away from the critical point alters where the terminal shock rests and how severely the flow delays and disturbed inside the intake [4].

1.2.6.2 Variable Geometry Inlets and CFD Based Optimization

Variable-geometry intake designs use moveable surfaces or cowl changes to stabilize shock structures and ensure proper pressure recovery across a wider Mach range. CFD-based optimization techniques have been applied to inlet systems operating at Mach 2.2 to 3, with a focus on how changes in cowl deflection angle affect mass flow, shock stability, and overall inlet efficiency. The simulations revealed that raising the deflection angle can effectively bring the oblique shock further forward, enhancing compression effectiveness at high Mach numbers, whereas smaller deflections reduce wave drag during lower-speed regions of the flight envelope. Further investigation of bleed-slot behavior revealed that optimal bleed location helps in the removal of low-energy boundary-layer air, avoiding shock-induced separation and ensuring subsonic diffuser stability. These results demonstrate how CFD-driven tweaking of variable-geometry inlets can increase the working Mach range and provide smoother transitions between different flight circumstances [7].

1.2.7 High Speed Wedge Flows and Detonation

1.2.7.1 Wedge Stabilized Oblique Detonation Waves

Wedge-stabilized oblique detonation waves (ODWs) are a combination of high-speed aerodynamics and reactive flow physics, with behavior influenced by both gas conditions and boundary-layer influences along the wedge. Multidimensional simulations of premixed hydrogen-air flow over single and double-angle wedges were used to determine how inflow Mach number, static temperature, wedge angle, and wedge length affect ODW formation. An ignition criteria was developed to relate these factors to whether an oblique shock will transition into a detonation wave and where along the wedge this transition happens, allowing for the prediction of ODW onset on inviscid wedges. The role of viscous effects was investigated using Mach 5 flow at inflow temperatures of 600, 700, and 800 K over a finite-length wedge with a boundary layer. At 600 K, the mixture ignites only within the boundary layer and does not ignite, whereas at 700 and 800 K, the burning boundary layer enhances the leading oblique shock sufficiently to initiate a stable ODW. The 800 K scenario results in a consistent leading-edge ODW, but the 700 K instance shows a cyclic pattern in which the ODW recedes and then reappears at the leading edge, which is linked to the interaction of underdriven detonation, induction-zone expansion, and separation-induced back pressure. These results reveal that boundary layers can significantly enhance shock strength, modify ignition locations, and even induce oscillatory detonation behavior, making them an important aspect in building wedge-based detonation and pressure-gain propulsion systems [5].

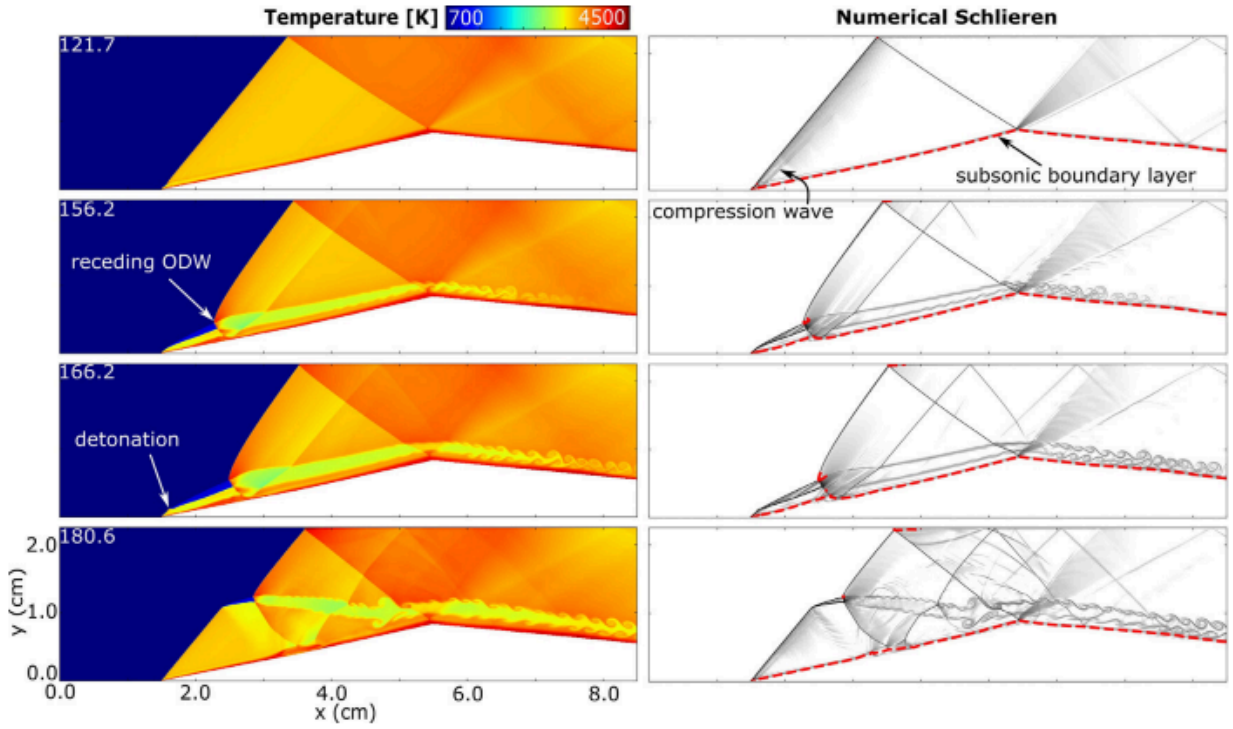


Figure 1.7 A viscous double-angle wedge in a Mach = 5, and T = 700 K flow. The subsonic region is enclosed by a dashed line. [5]

Figure 1.7 shows the unstable behavior of wedge-stabilized ODWs for a viscous double-angle wedge in a Mach 5, 700 K flow. The temperature fields on the left and numerical Schlieren representation on the right show a complete cycle of the quasi-stable mode. Early on, a CJ-like ODW anchors near the leading edge and enters the freestream, while a subsonic boundary layer forms along the wedge. As the burning boundary layer thickens, the leading shock and detonation structure weakens and moves downstream, resulting in the "receding ODW" stage and a building subsonic pocket along the wall. A compression wave develops from the induction zone and interacts with the boundary layer, eventually elevating the local back pressure sufficiently to cause a new detonation near the leading edge. The last frames show the fresh detonation re-establishing a strong ODW, resetting the process, and demonstrating the 700 K case's cyclic recession-redetonation characteristic [5].

1.3 Project Proposal

This research involves analyzing shock-wave behavior and flow parameters over F-16-inspired wedge geometries using MATLAB theoretical computations and Computational Fluid Dynamics (CFD) simulations. First, appropriate atmospheric and aircraft data will be used to determine the upstream freestream parameters of an F-16 Fighting Falcon in supersonic flight, including Mach number, velocity, static pressure, density, and temperature. Using these upstream conditions, two wedge configurations will be investigated, a single 15° wedge that generates one oblique shock and a double-wedge configuration with multiple deflection angles of 7.64° and

14.28°. For each configuration, MATLAB scripts will be used to calculate the theoretical downstream Mach number, velocity, pressure, density, and temperature at each shock, providing a clean, ideal reference based on compressible-flow relationships.

In parallel, 2D CFD models will be built to replicate the geometries and flow conditions. A 2D 15° wedge, patterned after the F-16 nose schematic from the flight handbook, will be built initially, followed by a modified double-wedge geometry derived from the original 15° wedge, with the first and second deflection angles set to 7.64° and 14.28°, respectively. Supersonic simulations at Mach 2 will then be performed for both scenarios. These simulations will yield contours and position-dependent plots of Mach number, velocity, static pressure, density, and temperature, with representative downstream values sampled at regions corresponding to the theoretical states.

Finally, theoretical and CFD results will be rigorously compared. Pressure differences between upstream and downstream regions for both wedge configurations will be assessed, and percent errors between theoretical and experimental (CFD) downstream values for all critical flow parameters will be calculated. This comparison will highlight the similarities and differences between ideal oblique-shock theory and numerical solutions, shedding light on the effects of geometry, numerical modeling, and potential flow non-ideal behaviors on shock structure and pressure recovery in supersonic inlet-like configurations.

1.4 Methodology

The approach consists of three phases that will help conduct this project and analyze the theoretical results with the experimental results of a supersonic 2D aircraft nose.

Supersonic Compressible Flow Setup and CFD Simulation

1. Gather theoretical upstream values and compute downstream values through Matlab
    a. Gather upstream properties of an F-16 Fighting Falcon such as Mach, Velocity, Pressure, Density, and Temperature.
    b. Gather properties of Mach, Velocity, Pressure, Density, and Temperature with respect to position of two wedge configurations:
        i. 1st wedge at 15 degrees creating one shock wave
        ii. 2nd wedge with two deflection angles at 7.64 degrees and 14.28 degrees
    c. Calculate theoretical downstream values of both Wedge configurations using Matlab.
2. Computational Fluid Dynamics Simulations
    a. Create the 2D Wedge at 15 degrees modeled after the F-16 nose schematic from the flight manual.
    b. Create and modify a double wedge from the original 15 degrees wedge, with the first deflection angle at 7.64 degrees and the second deflection angle at 14.28 degrees.
    c. Run a steady 2D inviscid CFD simulation at Mach 2 for both wedges.
    d. Gather plots and contours of Mach, Velocity, Pressure, Density, and Temperature all with respect to position and extract arbitrary downstream values.
3. Analyzing Results and Calculating Percent errors in Stagnation Pressures and Entropy

a. Gather Theoretical Stagnation Pressure and Entropy changes from upstream and downstream regions of both wedges and compare the percent error to the experimental downstream values of Stagnation Pressure and change in Entropy.

2 F-16 Fighting Falcon

2.1 Chapter Summary

This chapter offers a brief history of the F-16, tracing its roots to a lightweight fighter prototype program and its eventual adoption as a flexible tactical aircraft deployed by numerous countries. It describes the aircraft's main design elements, such as its single-engine layout, innovative flight control system, and overall configuration designed to improve mobility and combat effectiveness. The chapter also provides an overview of the F-16's typical armament and avionics system, demonstrating its multirole capabilities. Finally, it illustrates the fundamental external geometry and arrangement of the aircraft, utilizing a three-view image to highlight major components and reference stations that will be useful for this study.

2.2 F-16 Fighting Falcon Brief History

The F-16 originated from a new Air Force push for competing prototypes and a fly before buy strategy that began in 1971. The Lightweight Fighter program was approved in 1972, and two prototypes were built, the YF-16 and YF-17. The YF-16 went quickly through flight testing. It achieved Mach 2 in March 1974 and completed its demonstration program at the end of January 1975. The Air Force chose the YF-16 as the winner of the Air Combat Fighter competition in January 1975. The first prototype F-16 flew in December 1976, with the first production F-16A following in August 1978. The F-16 first entered service in the United States and Europe in 1979 and 1980, and it went on to be constructed in large numbers for over 25 countries while receiving regular improvements to keep it competitive [18]. The F-16A is a single engine, single seat, versatile tactical fighter (the F-16B is a tandem two-seat trainer). It has a huge bubble canopy, forebody strakes, an under-fuselage intake, thin moderately swept wings with automatic leading edge flaps, flaperons, and hydraulically powered controls controlled through a fly by wire system. Its fire control system combines radar, a HUD/REO display, and a stores management system. Standard weaponry includes a 20 mm gun with wingtip AAMs, as well as extra stores on underwing and centerline pylons. The manual also mentions the fly by wire flight control system, which provides static stability to reduce trim drag and improve maneuverability [19].

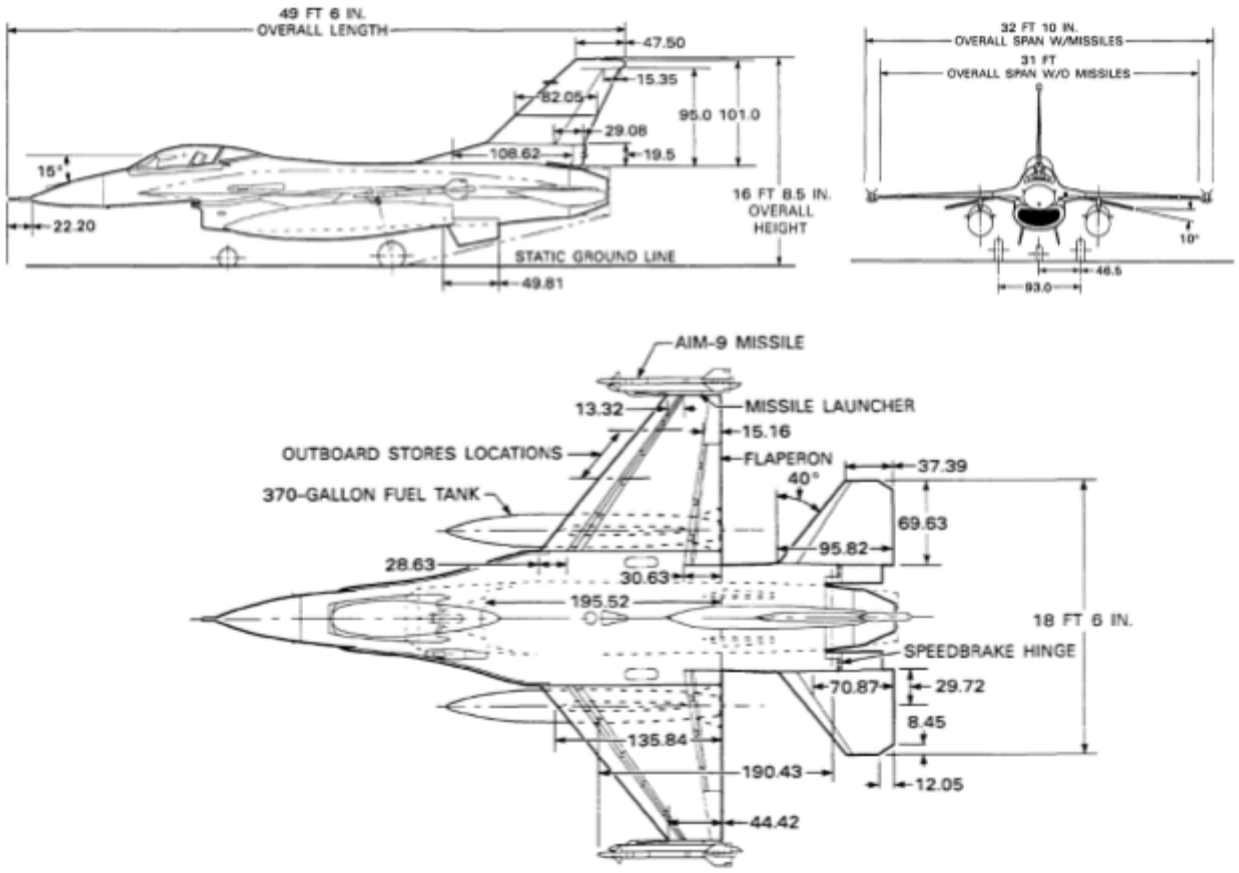


Figure 2.1 F-16 Dimension layout and equipment placement [19]

Figure 2.1 shows the F-16 is 49 feet 6 inches long, 16 feet 8.5 inches tall, and has a wingspan of 31 feet, which increases to 32 ft 10 in with wingtip missiles. The side view shows the ground line, a single belly air intake, and the nose gear in front of the main gear. The front view reveals the thin body and wingtip launch rails right above the intake. The top image shows the AIM-9 and its launcher at the tips, the outboard storage stations, and the 370-gallon tank beneath each wing. It also identifies the trailing edge flaperons and the rear fuselage speedbrake hinge. Inch station marks run throughout the wing and fuselage to indicate the precise location of pylons, hinges, and other components [19].

3 Theoretical Results

3.1 Chapter Overview

This chapter outlines the steps taken to calculate the theoretical flow field for both wedge shapes. Freestream conditions representative of an F-16 in supersonic flight were initially collected from publicly available sources. The NASA Glenn Earth Atmosphere Model, along with NASA information on Mach number, speed of sound, pressure, velocity, temperature and density provided the atmospheric state at the specified flight altitude [10, 11, 12]. The aircraft's operational altitude was derived from an official Air Force F-16 specification [13]. The dynamic viscosity of air was obtained from the material characteristics database in ANSYS Fluent. These upstream conditions were then plugged into a MATLAB script that generated standard oblique shock relations. For the single-wedge scenario, the code calculated downstream properties over the oblique shock generated by the 15^{o} nose-cockpit deflection shown in Figure 2.1 in Chapter 2. In the double-wedge instance, the same approach was used sequentially on the double wedge with two deflection angles at 7.64^{o} and 14.28^{o}, providing flow parameters downstream of the shocks. Finally, the MATLAB routine generated one-dimensional profiles and graphs of key variables such as Mach number, pressure, temperature, density, velocity, and dynamic pressure along the flow direction for both wedge configurations, providing a theoretical baseline for future comparison with CFD results.

3.2 Theoretical Upstream Values Calculations

Before any upstream flow parameters could be estimated, the thermodynamic constants for air needed to be determined. The ratio of specific heats (γ) and specific gas constant (R) were derived from conventional atmospheric air parameters used in compressible flow calculations. These constants govern how air responds to pressure and temperature changes, and they occur directly in the key equations employed in this research. The values of both (γ) and (R) are shown below in Figure 3.1 [11].

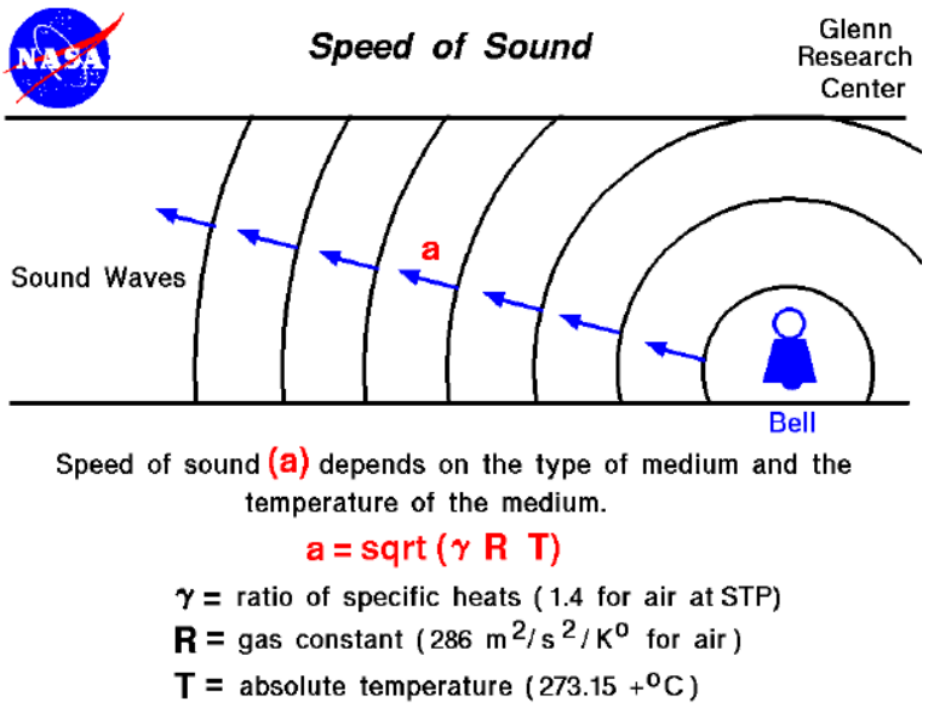


Figure 3.1 Values for specific heat ratio (γ) and gas constant (R) [11]

The operating altitude was determined using the U.S. Air Force F-16 performance data, which show a normal supersonic cruising condition of 50,000 feet [13]. This altitude, roughly 15,240 meters, was then fed into the NASA Earth Atmosphere Model to calculate the appropriate atmospheric conditions in Figure 3.2 [10]. This model yielded the ambient temperature, static pressure in Eqn 3.1, and density at 50,000 feet in Eqn 3.2 gathered from the literature modern compressible flow [6], which were used to determine the upstream atmospheric state for analysis. Once the temperature at that altitude was determined, it was utilized to calculate the local speed of sound in Eqn 3.3, establishing a consistent basis for defining the freestream Mach number and velocity used in theoretical computations in Eqn 3.4 and Figure 3.3. The Dynamic Pressure was computed using Eqn. 3.5.

$$P = 22.65 \cdot e^{(1.73-0.000157h)} \tag{3.1}$$

$$\rho = \frac{P}{RT} \tag{3.2}$$

$$a = \sqrt{\gamma \cdot R \cdot T} \tag{3.3}$$

$$M = \frac{V}{a} \tag{3.4}$$

$$q = \frac{1}{2}\rho V^2 \tag{3.5}$$

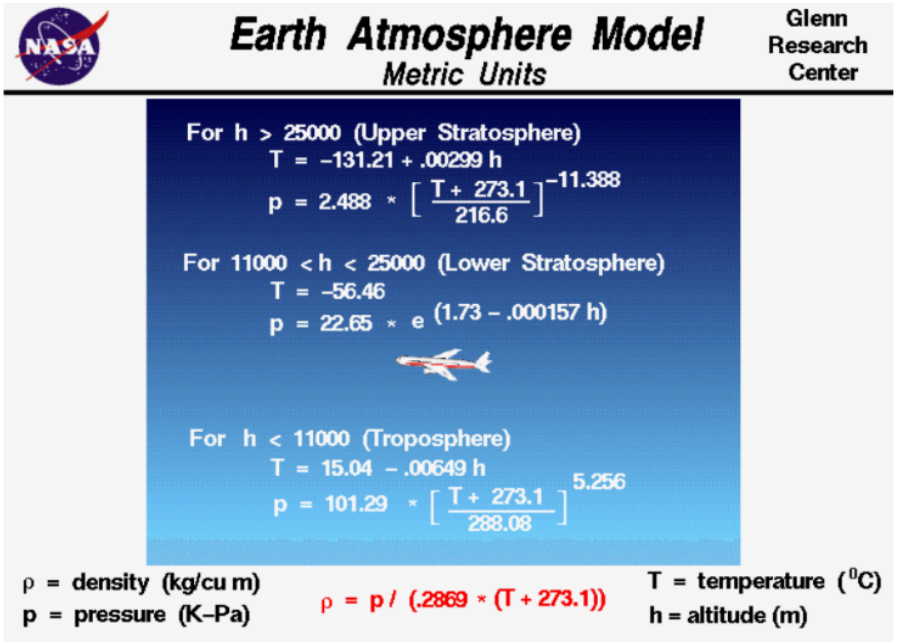


Figure 3.2 Earth atmosphere model [10]

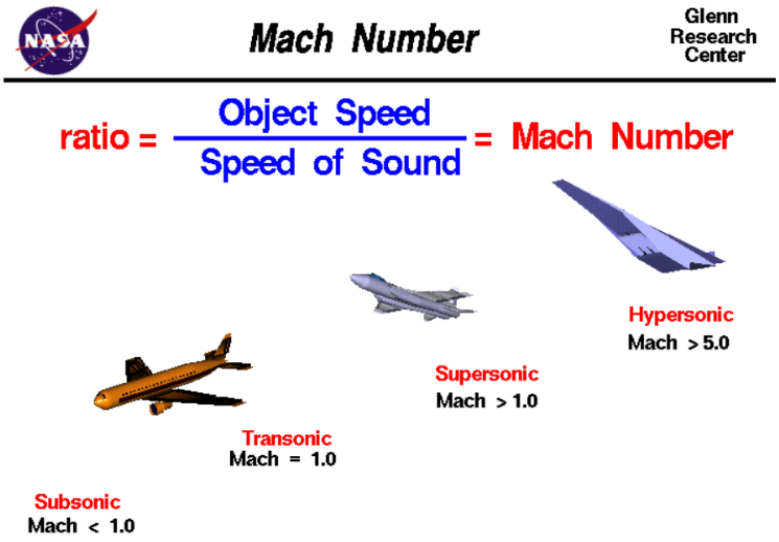


Figure 3.3 Mach number ratio [12]

All upstream flow parameters were derived through MATLAB by combining the chosen flight conditions with the governing compressible-flow relations depicted in the Figures and

Modern Compressible Flow textbook [6]. The findings are presented in Table 3.1. Starting with the chosen altitude and Mach number from F-16 performance data, the atmospheric model calculated the temperature and pressure at that height. Using these as a starting point, the remaining quantities such as density, speed of sound, freestream velocity, and dynamic pressure were computed step by step using the basic thermodynamic and fluid dynamic equations given in the methodology Figures. This procedure ensured that all upstream variables were obtained consistently from the same set of assumptions about the environment and gas properties.

Table 3.1 Upstream values specifications before shock

Definition	**Symbol**	**Value**	**Units**
Altitude	h	15,240	m
Gamma (Specific Heat Ratio)	γ	1.4	-
Gas Constant for Air	R	286	$\frac{J}{kg \cdot K}$
Speed of Sound	a1	294.555047	$\frac{m}{s}$
Mach	M1	2	-
Velocity	V1	589.110095	$\frac{m}{s^2}$
Temperature	T1	216.690000	K
Pressure	P1	11675.350820	Pa
Density	ρ1	0.188393	$\frac{kg}{m^3}$
Dynamic Pressure	q1	32690.982296	Pa

3.2.1 Theoretical Calculations for Wedge at 15^o

Figure 3.4 shows the upstream flow in Region 1 striking the 15^o wedge, resulting in an oblique shock wave attached to the leading edge. When the supersonic freestream meets the wedge, it is turned toward the surface, and the shock occurs at a fixed angle, separating the uniform upstream flow from the compressed downstream flow in Region 2. This downstream region behind the shock corresponds to the higher pressure, higher temperature, higher density, and lower Mach number values computed from the oblique and normal shock relations.

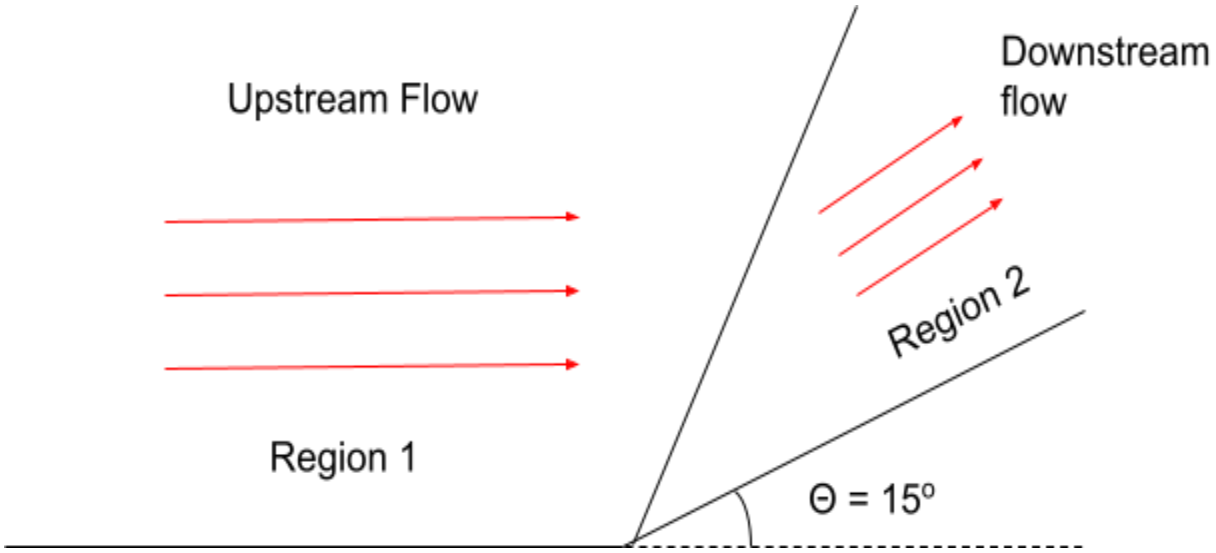


Figure 3.4 Oblique shock wave flow at 15° wedge

After obtaining the upstream values, The shock angle (β) was calculated using a compressible aerodynamics calculator [14]. However the downstream values can be calculated computationally by combining the wedge deflection angle with the upstream Mach number in the standard theta-beta-Mach formula for attached oblique shocks to determine the shock angle (β) in Eqn 3.6 [6].

$$tan\theta = \frac{2cot\beta\,(M1^2 sin^2\beta - 1)}{M1^2(\gamma + cos2\beta) + 2} \tag{3.6}$$

This shock angle was then used to calculate the component of the upstream Mach number normal to the shock, which is the quantity included in the normal shock relations in Eqn 3.7 [6].

$$Mn1 = M1\sin\beta \tag{3.7}$$

The normal shock equations used this upstream normal Mach number to calculate the pressure, density, and temperature ratios across the shock, as well as the downstream normal Mach number, which were all represented in terms of the normal component only shown in Eqns 3.9-3.11 [6].

$$\frac{\rho 2}{\rho 1} = \frac{(\gamma+1)Mn1^2}{2+(\gamma-1)Mn1^2} \tag{3.8}$$

$$\frac{P2}{P1} = 1 + \frac{2\gamma}{\gamma-1}(Mn1^2 - 1) \tag{3.9}$$

$$\frac{T2}{T1} = \frac{(\frac{P2}{P1})}{(\frac{\rho 2}{\rho 1})} \tag{3.10}$$

$$Mn2^2 = \frac{1+\frac{\gamma-1}{2}Mn1^2}{\gamma Mn1^2-\frac{\gamma-1}{2}} \tag{3.11}$$

The complete downstream Mach number aligned with the turned flow was then calculated by projecting the downstream normal Mach number back into the flow direction following flow deflection in Eqn 3.11 [6].

$$M2 = \frac{Mn2}{sin(\beta - \theta)} \tag{3.11}$$

These shock-derived ratios were applied to the upstream static pressure, temperature, and density to determine the downstream static pressure, temperature, and density in Region 2 using Eqns 3.12-3.14 [6].

$$P2 = P1(\frac{P2}{P1}) \tag{3.12}$$

$$T2 = T1(\frac{T2}{T1}) \tag{3.13}$$

$$\rho 2 = \rho 1(\frac{\rho 2}{\rho 1}) \tag{3.14}$$

The downstream speed of sound was then calculated using the perfect-gas relation and combined with the downstream Mach number to yield the downstream flow velocity all mentioned in section 3.2 using Eqns 3.3-3.5 [6].

The isentropic stagnation pressure relation in Eqn 3.15 was applied independently in the upstream and downstream regions to obtain the corresponding stagnation pressures and their ratio, which were then used to calculate the total-pressure across the oblique shock in Eqn 3.16. The Entropy change across the shock was calculated using Eqn 3.17 [6].

$$P0i = Pi(1 + \frac{\gamma-1}{2}Mi^2)^{\frac{\gamma}{\gamma-1}}, \quad i = 1, 2, 3..... n \tag{3.15}$$

$$\frac{P02}{P01} \tag{3.16}$$

$$\Delta S = -R ln\left(\frac{P02}{P01}\right) \quad (3.17)$$

Table 3.2 presents the downstream flow data derived from the oblique shock study, including the calculated Mach number, velocity, static pressure, temperature, density, dynamic pressure, and stagnation pressure ratio using the methods discussed.

Table 3.2 Theoretical downstream values after shock at 15°

Definition	Symbol	Value	Units
Altitude	h	15,240	m
Gamma (Specific Heat Ratio)	γ	1.4	-
Gas Constant for Air	R	286	$\frac{J}{kg \cdot K}$
Speed of Sound	a2	331.865168	$\frac{m}{s}$
Mach	M2	1.445716	-
Velocity	V2	479.782904	$\frac{m}{s}$
Temperature	T2	275.061163	K
Pressure	P2	25623.345263	Pa
Density	ρ2	0.325717	$\frac{kg}{m^3}$
Dynamic Pressure	q2	37488.672573	Pa
Stagnation Pressure Ratio from region 1 to 2	$\frac{P02}{P01}$	0.952356	-
Total Entropy from region 1 to 2	$\Delta S_{1\rightarrow 2}$	13.96148025	$\frac{J}{kg \cdot K}$

From Region 1 to Region 2, The post-shock Mach number drops drastically, indicating less powerful but still supersonic flow. The Mach number falls from 2.00 to around 1.45, and the velocity decreases by about 19%, but the speed of sound increases as the static temperature rises from about 217 K to 275 K. Both static pressure and density increase dramatically over the shock, pressure by more than a factor of two and density by approximately 73%, indicating compressive shock behavior [6]. Even though the velocity reduces, the combination of higher

density and fairly high speed leads the dynamic pressure to increase slightly from 3.27×10^4 Pa to 3.75×10^4 Pa, representing a denser but somewhat slower supersonic flow downstream of the oblique shock.

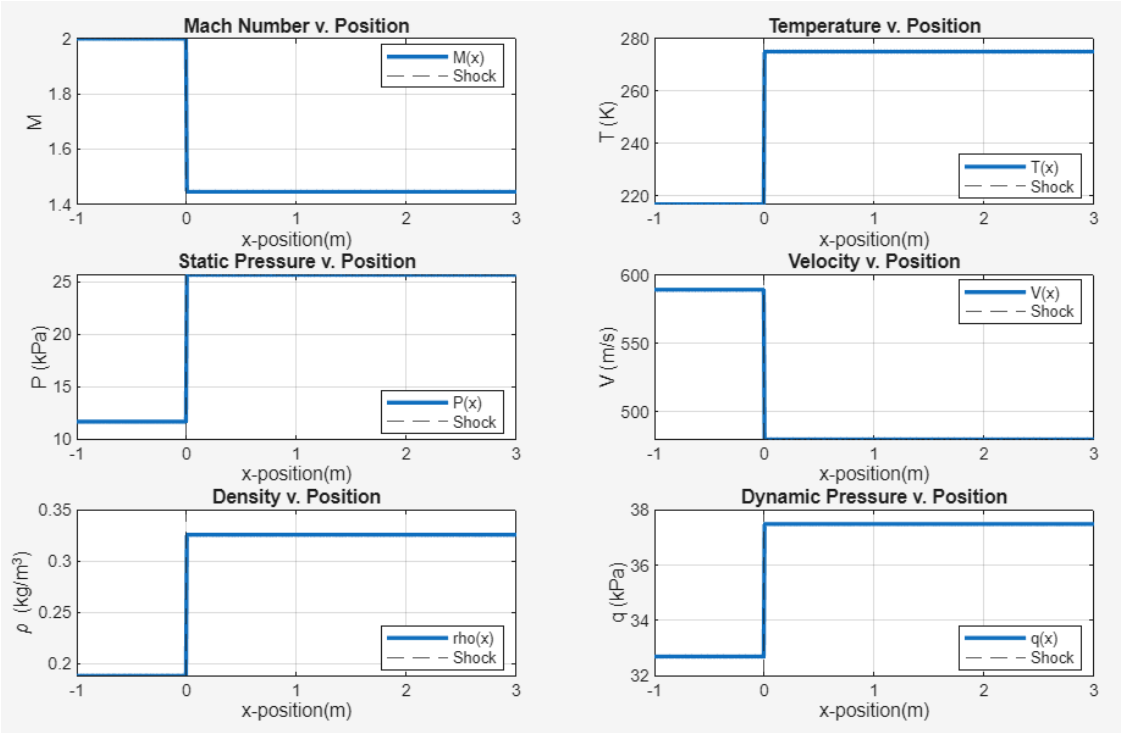


Figure 3.5 Matlab graphs of flow properties across shock at 15° (theoretical)

Figure 3.5 illustrates the upstream and downstream nature of the properties. Before the shock, each plot shows a uniform freestream with a high supersonic speed of around 590 m/s, comparatively low temperature about 217 K, low pressure near 11.7 kPa, low density about 0.19 kg/m³, and a dynamic pressure little over 32 kPa. At the shock, all curves jump abruptly, indicating the discontinuity predicted by the MATLAB calculations. The flow decreases but remains supersonic, speed drops to approximately 480 m/s, while temperature, pressure, and density all increase sharply to about 275 K, 25.6 kPa, and 0.33 kg/m³, respectively. The dynamic pressure also rises to at 37.5 kPa, indicating the combined effect of a denser but slower flow downstream. These step changes in the graphs correspond closely to the upstream and downstream values generated by the computational oblique shock analysis in table 3.1 and 3.2.

3.2.2 Theoretical Calculations for Double Wedge at 7.64° and 14.2°

The relations outlined in Equations 3.6-3.17 were utilized to derive the downstream values for the double-wedge configuration, which was the same technique as for the single wedge. In this example, the flow first passes over the first wedge at 7.64° , where the deflection angle and upstream Mach number are combined with the theta-beta-Mach and normal-shock relations to calculate the first set of downstream characteristics in Region 2. These Region 2 values are then used as the new "upstream" state for the second wedge at 14.28°, where the

identical equations are used again to generate the final downstream properties behind the second shock in Region 3. The only change from the single-wedge situation is that the operation is repeated twice in sequence to account for two shocks rather than one. The angles were chosen arbitrarily. The Flow illustration is shown in Figure 3.6.

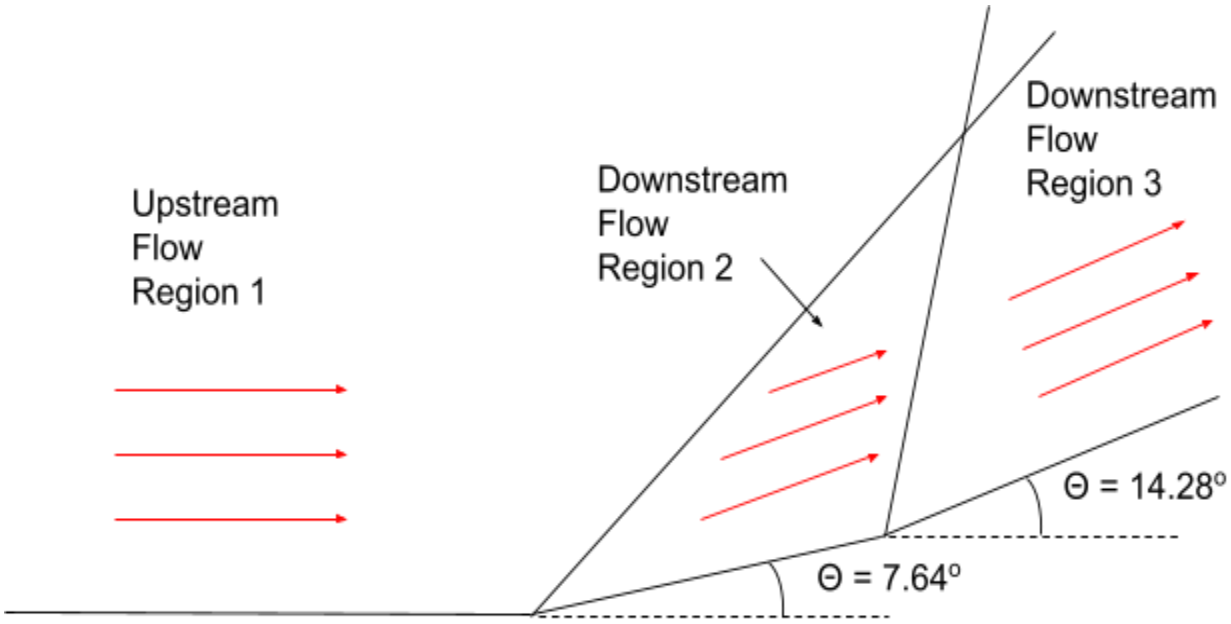


Figure 3.6 Oblique shock wave flow of double wedge at 7.64° and 14.2°

Tables 3.3 and 3.4 represent downstream flow values over the two shocks produced by the double-wedge configuration, highlighting the changes in flow parameters following the first shock in Region 2 and the second shock in Region 3.

The results show how the flow is gradually compressed as it goes through the two shocks and across the double wedge. Following the first shock, the speed of sound, temperature, static pressure, density, and dynamic pressure all increase in comparison to the upstream freestream, while the Mach number decreases but the flow remains clearly supersonic. The associated stagnation-pressure loss and entropy rise are small, indicating a weak first shock. The flow is squeezed considerably more downstream of the second shock. The Mach number approaches 1, the velocity declines, and the temperature, static pressure, and density climb significantly higher than after the first shock.

Table 3.3 Theoretical downstream values after shock at 7.64°

Definition	**Symbol**	**Value**	**Units**
Altitude	h	15,240	m
Gamma (Specific Heat Ratio)	γ	1.4	-

Gas Constant for Air	R	286	$\frac{J}{kg \cdot K}$
Speed of Sound	a2	312.780846	$\frac{m}{s}$
Mach	M2	1.726759	-
Velocity	V2	540.097025	$\frac{m}{s}$
Temperature	T2	244.335308	K
Pressure	P2	17647.141167	Pa
Density	ρ2	0.252535	$\frac{kg}{m^3}$
Dynamic Pressure	q2	36832.879378	Pa
Stagnation Pressure Ratio from region 1 to 2	$\frac{P02}{P01}$	0.992861	-
Total Entropy from region 1 to 2	$\Delta S_{1\rightarrow 2}$	2.049076914	$\frac{J}{kg \cdot K}$

Table 3.4 Theoretical downstream values after shock at 14.28°

Definition	**Symbol**	**Value**	**Units**
Altitude	h	15,240	m
Gamma (Specific Heat Ratio)	γ	1.4	-
Gas Constant for Air	R	286	$\frac{J}{kg \cdot K}$
Speed of Sound	a3	348.571029	$\frac{m}{s}$
Mach	M3	1.194475	-
Velocity	V3	416.359546	$\frac{m}{s}$
Temperature	T3	303.450955	K
Pressure	P3	36278.802447	Pa

Density	ρ3	0.418021	$\frac{kg}{m^3}$
Dynamic Pressure	q3	36233.097072	Pa
Stagnation Pressure Ratio from region 2 to 3	$\frac{P03}{P02}$	0.962987	-
Stagnation Pressure Ratio from region 1 to 3	$\frac{P03}{P01}$	0.956113	-
Total Entropy from region 2 to 3	$\Delta S_{2\rightarrow3}$	10.78659489	$\frac{J}{kg \cdot K}$
Total Entropy from region 1 to 3	$\Delta S_{1\rightarrow3}$	10.15588461	$\frac{J}{kg \cdot K}$

Figure 3.7 shows the theoretical Matlab graphs of the spatial fluctuation of important flow parameters as the freestream passes through two oblique shocks on the nose. Upstream of the initial shock, the Mach number and velocity remain high and fairly uniform, but the static pressure, density, temperature, and dynamic pressure are all relatively low and nearly constant. At the first shock location, all plots show a clear step change, Mach number and velocity fall, while static pressure, density, temperature, and dynamic pressure rise to new uniform levels in the first downstream region. A second, similar discontinuity is seen at the location of the second shock. The Mach number and velocity decrease further, while static pressure, density, and temperature reach their peak levels, with a more minor shift in dynamic pressure. Overall, the image depicts how the two shocks behave as distinct compression waves, gradually decreasing and heating the flow while increasing its pressure and density along the nose.

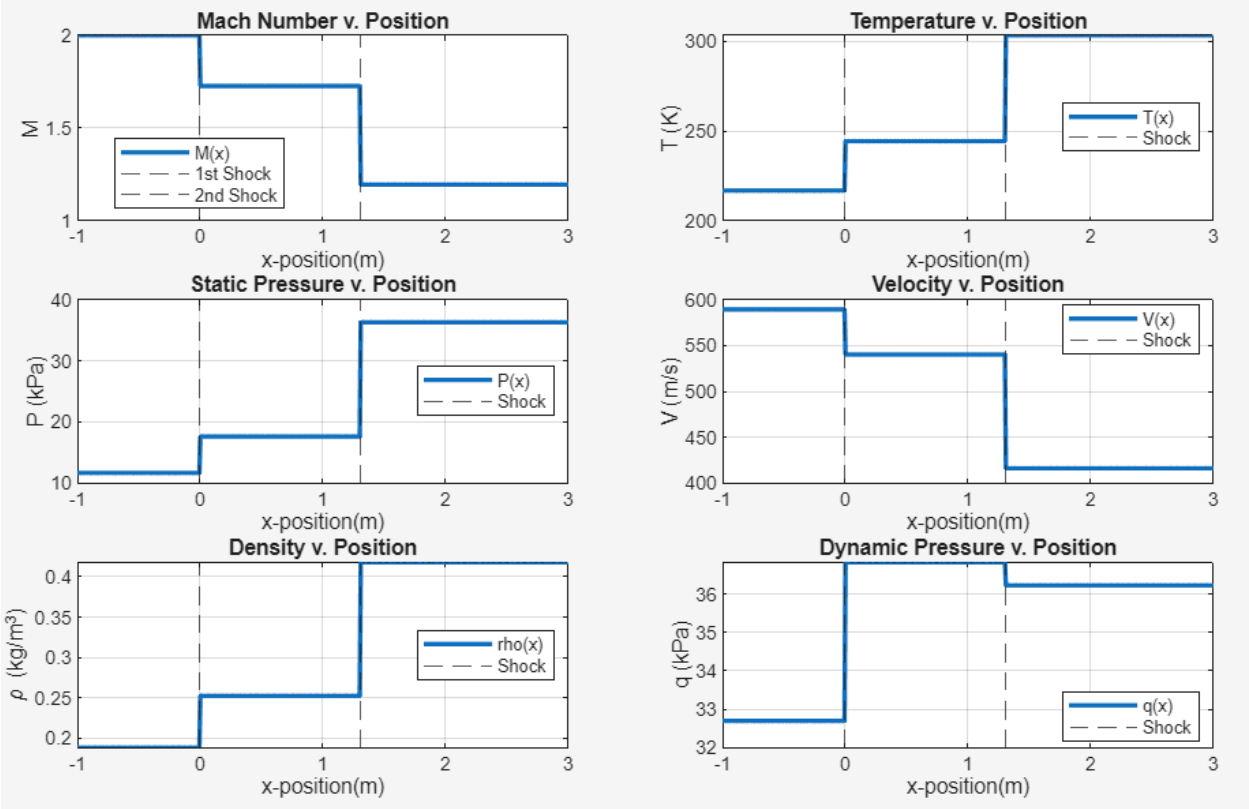


Figure 3.7 Matlab graphs of flow properties across shocks at 7.64º and 14.2º (theoretical)

3.3 Entropy Change and Stagnation Pressure Ratio of Both Wedges

In compressible-flow theory, the perfect or ideal condition is one in which the flow is adiabatic and totally reversible, resulting in no change in entropy or loss of stagnation (total) pressure as the fluid travels through the system. In that instance, the total pressure measured along a streamline is constant everywhere, implying that the flow goes through without friction, shocks, or other irreversibilities that might limit its ability to generate meaningful work. When entropy increases, such as over a shock wave or in a highly viscous region, total pressure declines, which is a clear indication of how much performance or efficiency has been lost in comparison to this ideal, loss-free benchmark [6].

Table 3.5 compares the total entropy and total stagnation pressure changes between the single 15º wedge and the double wedge with shocks at 7.64º and 14.28º. These values are used to compare the amount of irreversibility and total-pressure loss produced by each configuration, as well as how near it is to the ideal case in which entropy remains constant and total pressure is preserved. The project determines which wedge configuration provides more efficient supersonic compression based on the theoretical framework by directly comparing the losses for the single shock and the two-shock system.

Table 3.5 Comparison of theoretical total stagnation pressure and entropy in single and double wedge configurations

Configuration	**Angle in Degrees**	**Stagnation Pressure across System (Total Pressure)**	**Entropy of System**
Single Wedge	15^o	$\frac{P02}{P01} = 0.952356$	$\Delta S_{1\rightarrow2} = 13.96148025$
Double Wedge	7.64^o and 14.28^o	$\frac{P03}{P01} = 0.956113$	$\Delta S_{1\rightarrow3} = 10.15588461$
Percent Change		+0.956113%	-27.26%

Based on the results, the stagnation pressure ratio for the single wedge is 0.952356, with an entropy rise of 13.96 J/(kg·K). This indicates a significant loss of total pressure and a high level of irreversibility across the system. The double wedge (7.64^o and 14.28^o) improves the stagnation pressure ratio to 0.956113 and reduces entropy increase to 10.16 J/(kg·K), resulting in a 0.956113% improvement in total pressure conservation and a 27.26% reduction in entropy generation. Because ideal isentropic compression has a stagnation pressure ratio of 1 and zero entropy change, these results suggest that the double-wedge configuration functions closer to the ideal case and is accordingly the more efficient of the two geometries.

4 Experimental Results

4.1 Chapter Overview

This chapter describes the experimental results of supersonic flow over a single 15° wedge and a double-wedge configuration. It begins by describing the geometry of the wedges and the test domain, followed by a description of how the mesh is formed and refined in shock-prone places. The experimental setup is then described, including the operating conditions in chapter 2 and techniques used to collect data for both the single wedge at 15° and the 7.64° and 14.28° double wedge. Finally, the measured flow fields are evaluated to identify the related changes in entropy and stagnation pressure for each design, allowing for a comparison of their total compressive efficiency.

4.2 Geometry

The wedge geometry was first approximated in SolidWorks by importing the F-16 side profile, drawing over the nose portion, and measuring the length of the inclined face with the sketch tools, providing an effective nose length of about 2.61 meters. The reference length was then utilized to generate the single-wedge model in ANSYS DesignModeler. By setting the nose tip at the origin and defining a horizontal reference axis of 2.61 m, the wedge surface was produced by connecting the origin to the circle at an angle of approximately 345° in the sketch, equal to a 15° inclination from the horizontal. The double wedge configuration was created by modifying this baseline sketch, a break point was introduced roughly midway along the nose, and a second straight segment was added, resulting in an effective deflection of about 7.64° for the first segment and 14.28° for the second segment, while the overall length remained 2.61 m. To correctly constrain the geometry, the horizontal offset of the break point is about 1.305m and two step heights approximately 0.35m and 0.70m were chosen. Both the single wedge and double wedge values are all approximations. These sketches are represented in Figure 4.1.

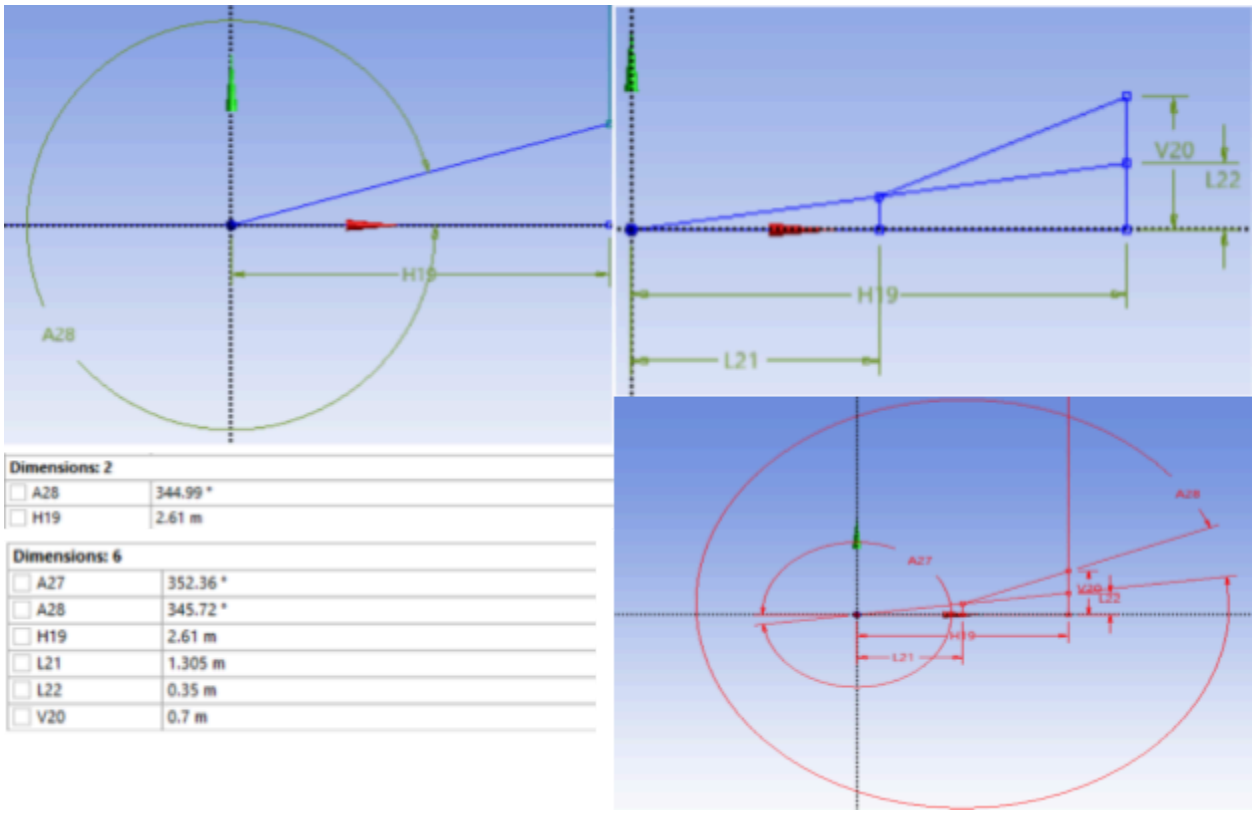


Figure 4.1 Sketch of single and double wedge on ANSYS design modeler

4.3 Mesh Setup

The mesh generation process for both the single-wedge and double-wedge variants uses a structured, mapped approach to ensure high-quality resolution of the supersonic flow field. The wedges are placed in a 2D planar rectangular farfield domain, and the fluid region is partitioned with straight dividing lines, resulting in basic four-sided faces ideal for mapping face meshing with primarily orthogonal quadrilateral elements. A body sizing control is applied to the fluid surface to ensure that element sizes are uniform across the domain, resulting in consistent spatial resolution in both upstream and downstream regions of the shock system. The geometry is then separated into named selections that correspond to the wedge wall, inlet, outlet, and farfield boundaries, allowing for the clear and systematic assignment of boundary conditions in the CFD solver. Using the same meshing process for both single and double wedge configurations assures that changes in results are mostly caused by geometric and shock structure effects, rather than variations in mesh topology or quality [15]. The meshing of both wedges along with the names selections is shown in Figure 4.2 [15].

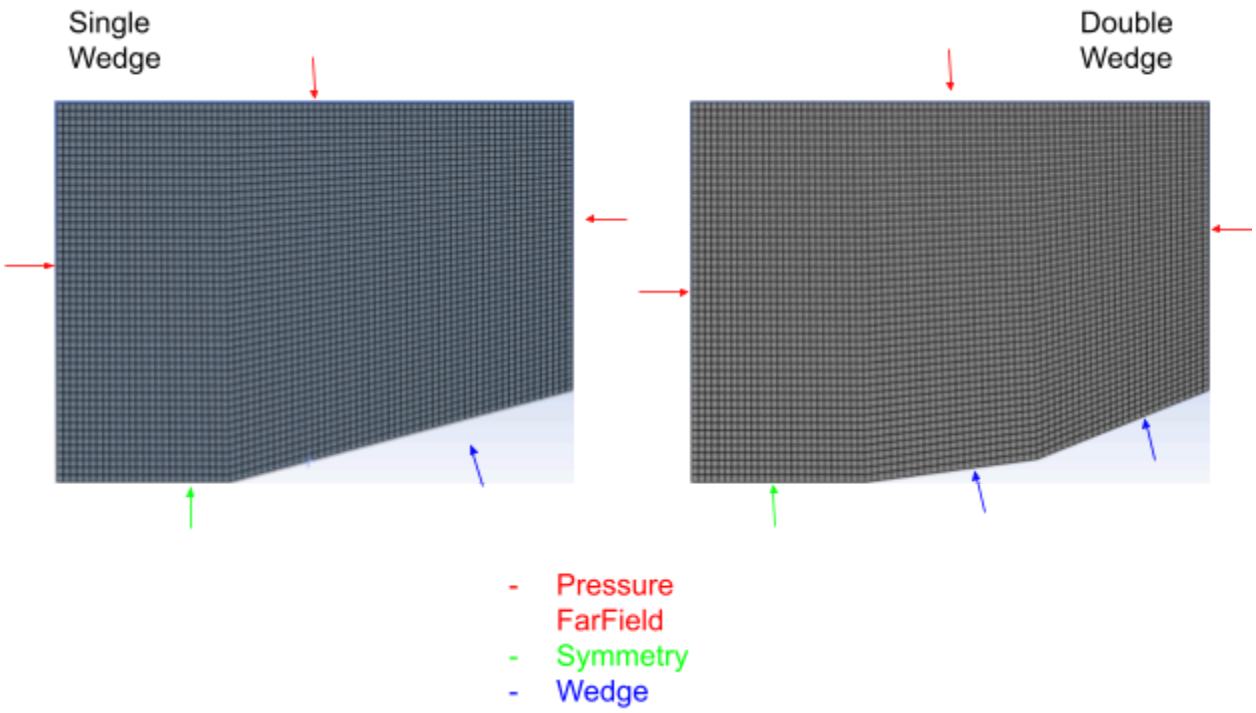


Figure 4.2 Mesh and named selections of single wedge and double wedge

4.4 CFD Setup

The CFD simulations in ANSYS Fluent for both the single-wedge and double-wedge configurations were carried out with a reliable, two-dimensional, density-based solver designed for high-speed compressible flow. The energy equation was turned on and the viscous model was set to inviscid. Air was modeled as an ideal gas with C_p = 1006.43 J/(kg*K) and a molecular weight of 28.966 kg/kg·mol. Density was calculated based on the local pressure-temperature field. A pressure far-field boundary condition specified the freestream at a gauge pressure of 11,675 Pa, Mach number 2, and static temperature of 216.69 K, with the wedge surface defined as a wall and the remaining outer boundary treated as symmetry, the operating pressure was set to zero gauge to ensure that all pressures in the domain corresponded to physical values. The pressure far-field boundary provided reference values for nondimensional parameters, and the convective terms were spatially discretized using a second-order upwind approach. The Courant number was set to 5.0 in the density-based implicit formulation to achieve a balance between convergence rate and numerical stability. The solution was initialized using standard initialization with the initial state computed from the farfield boundary. Convergence was monitored by tightening the absolute residual criteria for continuity, x- and y-momentum, and energy to 10^{-14}, followed by running 2000 iterations to achieve a steady solution. After convergence, contours and graphs of static pressure, dynamic pressure, density, temperature, velocity magnitude, and Mach number were collected to study the shock structure and compare the single and double wedge scenarios.

For an accurate assessment, the experimental calculations will use the same upstream values shown in table 3.1. The downstream values of both the single wedge and double wedge will be approximated and used to calculate the total Pressure ratios and the change in entropy.

4.4.1 Experimental Results for 15° Wedge

In the single-wedge case in Figure 4.3, the residuals plot shows a rapid and linear decrease of all equations (continuity, x-velocity, y-velocity, and energy) over the first 150 iterations, dropping from order 10^{0} to approximately 10^{-3}, indicating that the initial transients are effectively damped out and the solution approaches a steady state. After this point, the residuals level out and show minor, periodic oscillations around the 10^{-3} range. This behavior is typical of density-based stable simulations with powerful shocks, where the discrete shock position oscillates slightly over a few cells. The close grouping of the continuity, momentum, and energy residuals, as well as the lack of a long-term growth trend, indicate that the solver has arrived at a statistically stable solution, with remaining fluctuations due to the shock-capturing process rather than global divergence.

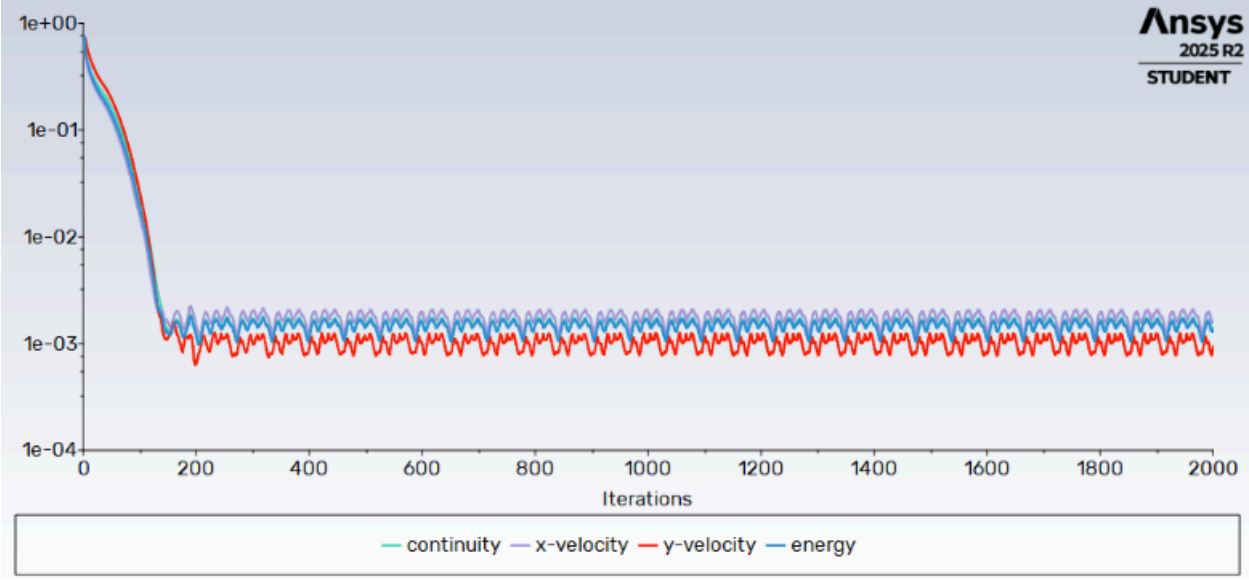


Figure 4.3 Residuals plot (single wedge)

The plots in Figure 4.4 shows both the static pressure and the dynamic pressure distribution on the single-wedge surface as a function of streamwise position.

Starting at the leading edge, the static pressure rises quickly from the freestream value of 1.6×10^{4} Pa to a high value of roughly 2.7×10^{4} Pa right downstream of the compression corner. This corresponds to the pressure leap across the oblique shock attached to the wedge. After the peak, the pressure decreases slightly and then remains approximately constant at around 2.55×10^{4} Pa over the rest of the wedge surface. This indicates that the post-shock flow along the plate is nearly uniform and that no major pressure gradients are present downstream of the shock interaction region.

The dynamic pressure distribution across the same wedge surface. Similar behavior is observed, the dynamic pressure increases abruptly from its upstream value of about 3.45×10^4 Pa to a high of nearly 3.70×10^4 Pa near the leading edge, representing the combined effect of the velocity and density changes over the oblique shock. After the overshoot, the dynamic pressure lowers somewhat and stabilizes around 3.68×10^4 Pa for the remaining length of the wedge. The virtually flat downstream profile indicates that, once the flow has passed through the shock and been adjusted, the post-shock region over the wedge is close to a uniform supersonic condition, with only tiny differences caused by boundary-layer development and numerical shock-capturing effects.

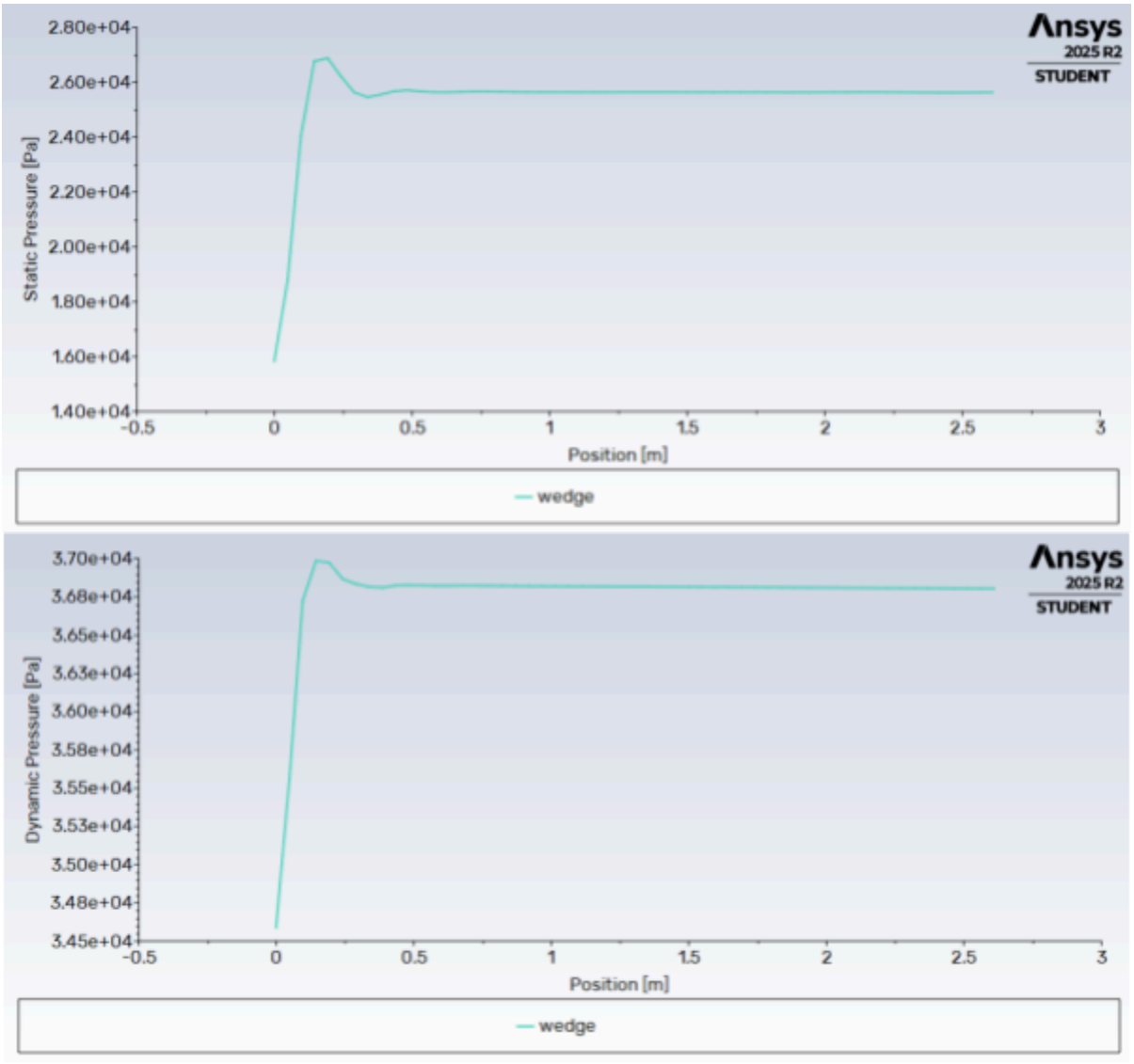


Figure 4.4 Static pressure and dynamic pressure plots (single wedge)

The plots in Figure 4.5 shows both the static temperature and density distribution throughout the same wedge surface.

A similar trend is observed, static temperature increases significantly from the freestream value of around 2.42×10^{2} K to a maximum of 2.80×10^{2} K just downstream of the leading edge. This reflects the significant compressive heating associated with the oblique shock. After a minor decline, the temperature stabilizes around 2.74×10^{2} K along the wedge. The relatively uniform downstream temperature distribution demonstrates that the shock causes the primary thermodynamic change, but the flow across the wedge surface downstream of the interaction remains close to a steady post-shock condition.

The density distribution along a single wedge surface. The density rises sharply along the leading edge, from 2.3×10^{-1} kg/m3 upstream to a peak of 3.35×10^{-1} kg/m3, indicating significant compression across the oblique shock of the wedge. After the peak, the density decreases slightly and remains steady at around 3.2×10^{-1} kg/m3 for the rest of the wedge. This plateau implies that, after the shock, the flow along the surface settles into a relatively uniform post-shock state with just small deviations, which is compatible with a continuous supersonic external flow across a simple compression ramp.

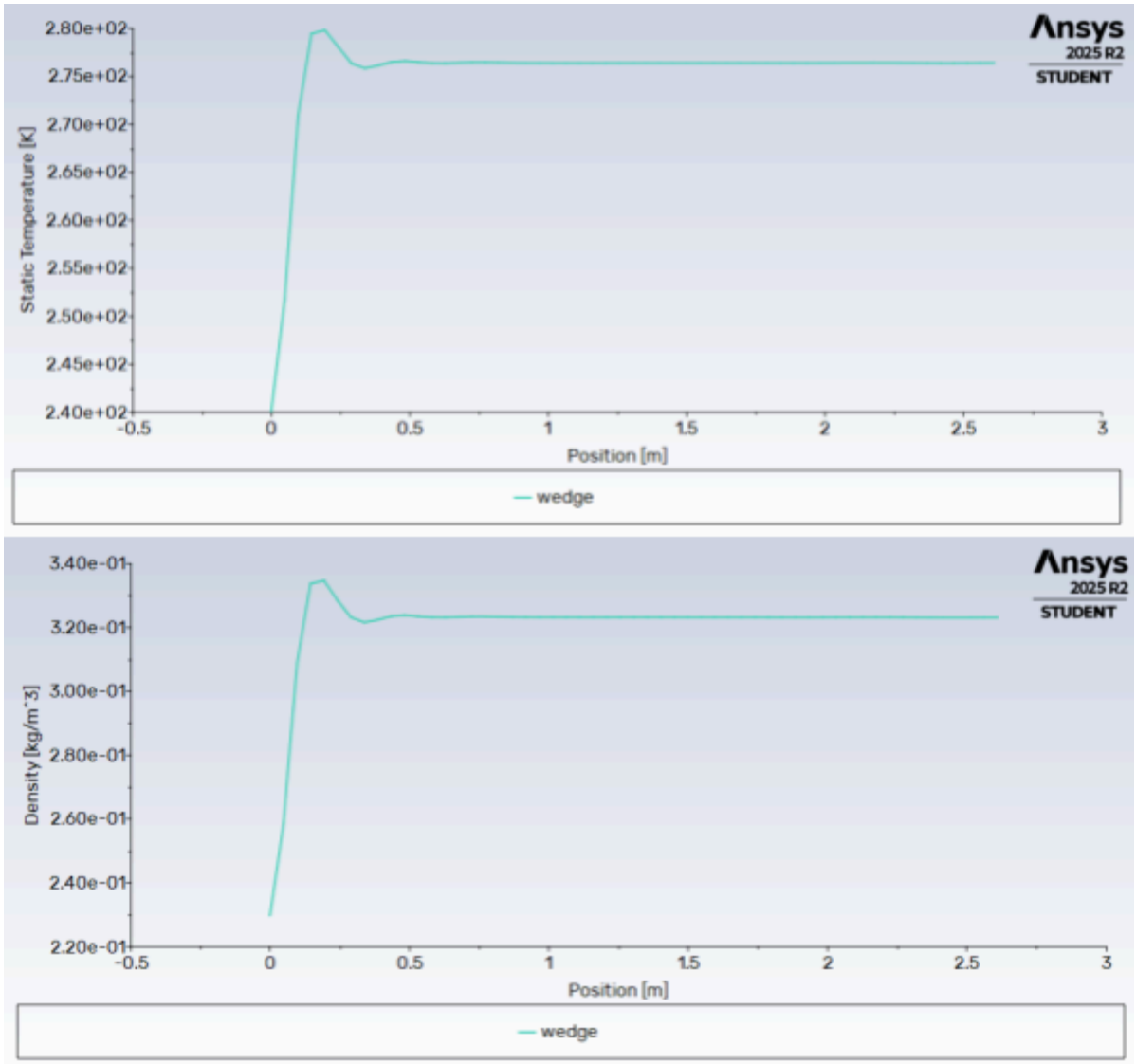


Figure 4.5 Static temperature and density plots (single wedge)

The plots in Figure 4.6 show both the velocity magnitude and mach distribution along a single-wedge surface.

The velocity declines from 5.9×10^2 m/s upstream to 4.6×10^2 m/s at the leading edge, indicating significant decrease due to the oblique shock. Following the rapid reduction, the velocity stabilizes at 4.75×10^2 m/s for the remainder of the wedge. The relatively flat downstream region of the curve implies that the post-shock flow over the surface is largely uniform.

The Mach number distribution across the same wedge surface. A similar pattern emerges, the Mach number rapidly declines from the freestream value of 2 to around 1.4 just past the leading edge, representing the transition from a higher-Mach upstream state to a weaker, but still supersonic, postshock state. Downstream of this sharp decrease, the Mach number shows a tiny overshoot before leveling off around 1.42-1.43 for the remainder of the wedge. This somewhat

constant downstream Mach level demonstrates that the principal compressive occurrence takes place at the oblique shock, and the flow settles into a stable, uniform supersonic regime over the wedge surface.

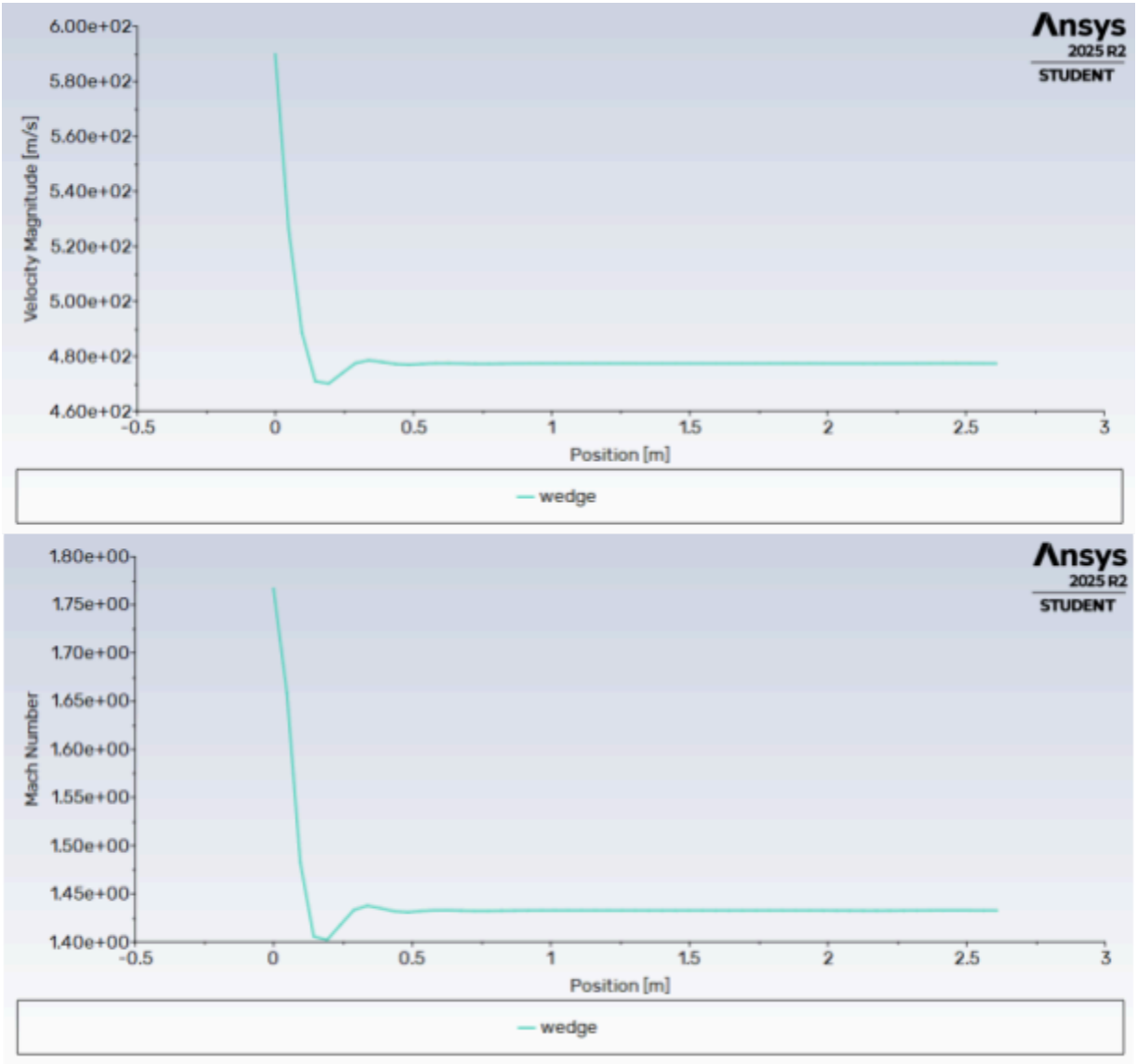


Figure 4.6 Velocity magnitude and Mach plots (single wedge)

The CFD results for the single-wedge scenario are in extremely close alignment with the MATLAB oblique-shock solution, both qualitatively and numerically. The Fluent surface plots for each variable, Mach number, static pressure, density, dynamic pressure, velocity, and temperature show the identical upstream plateau, dramatic jump at the shock, and almost uniform downstream plateau as the 1D MATLAB graphs in Figure 3.5. The upstream and

downstream levels closely match the predicted values, with only minor differences such as small overshoots and a smoothed shock region in the CFD curves.

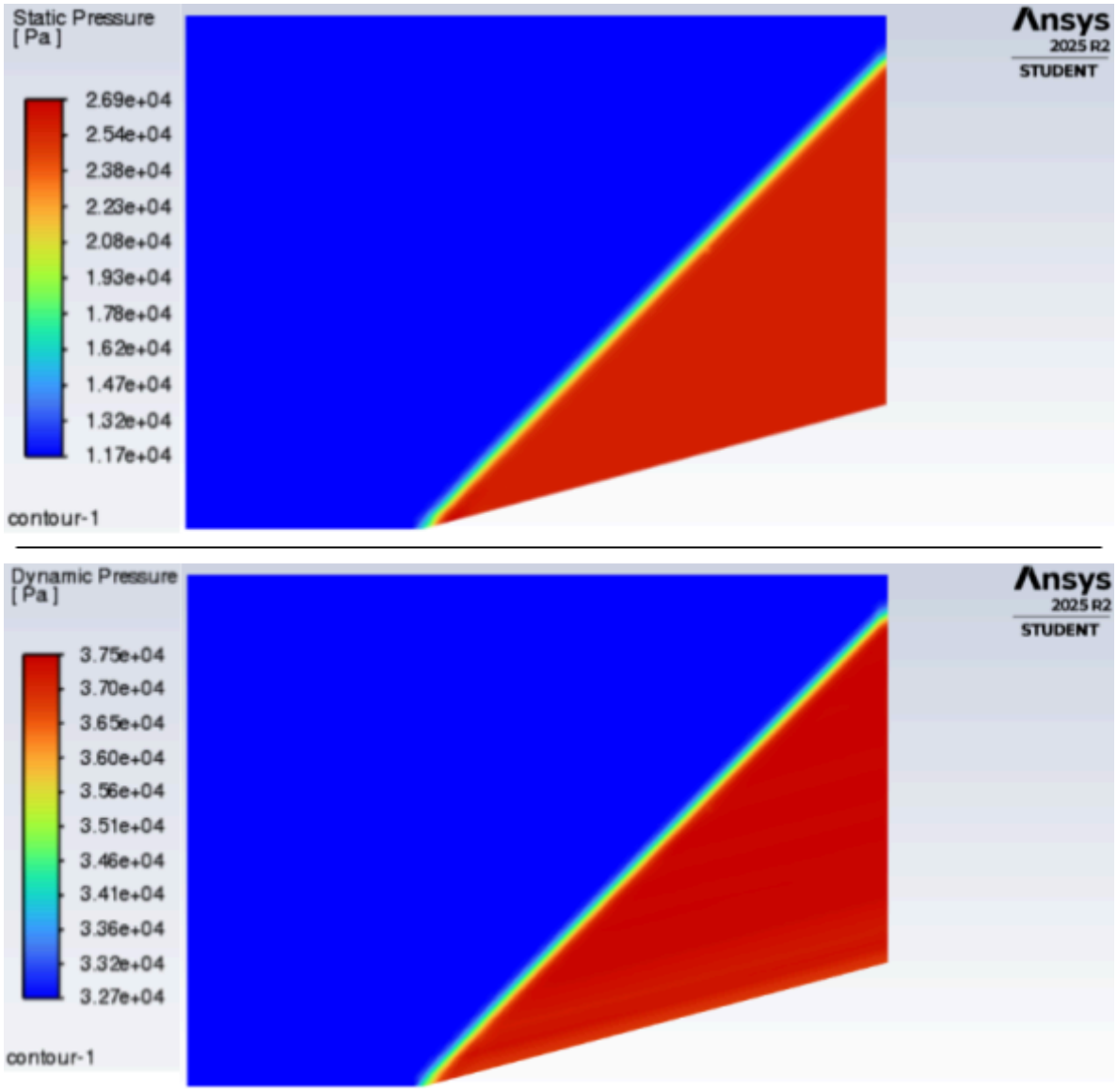


Figure 4.7 Static pressure and dynamic pressure contours (single wedge)

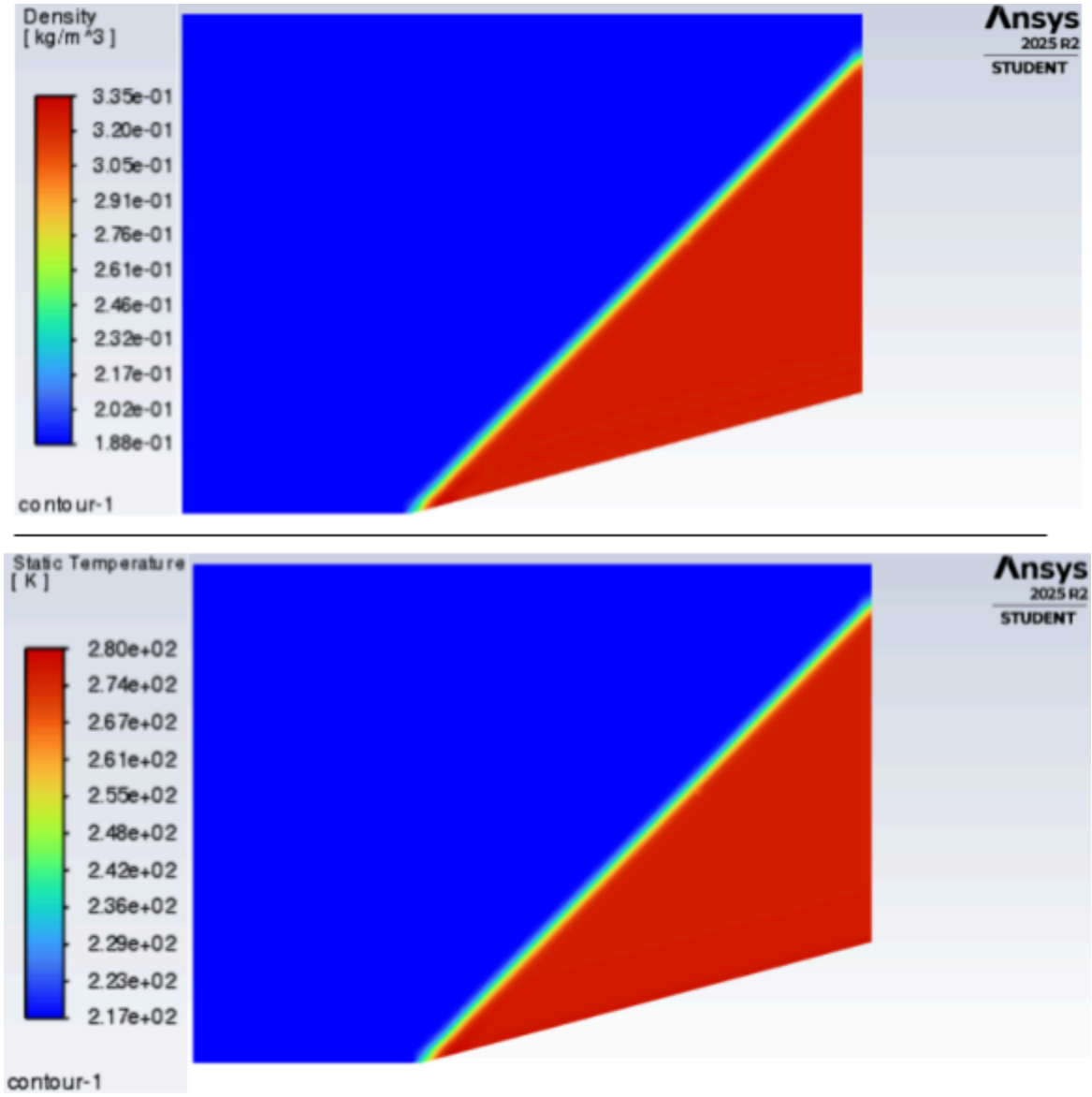


Figure 4.8 Static temperature and density contours (single wedge)

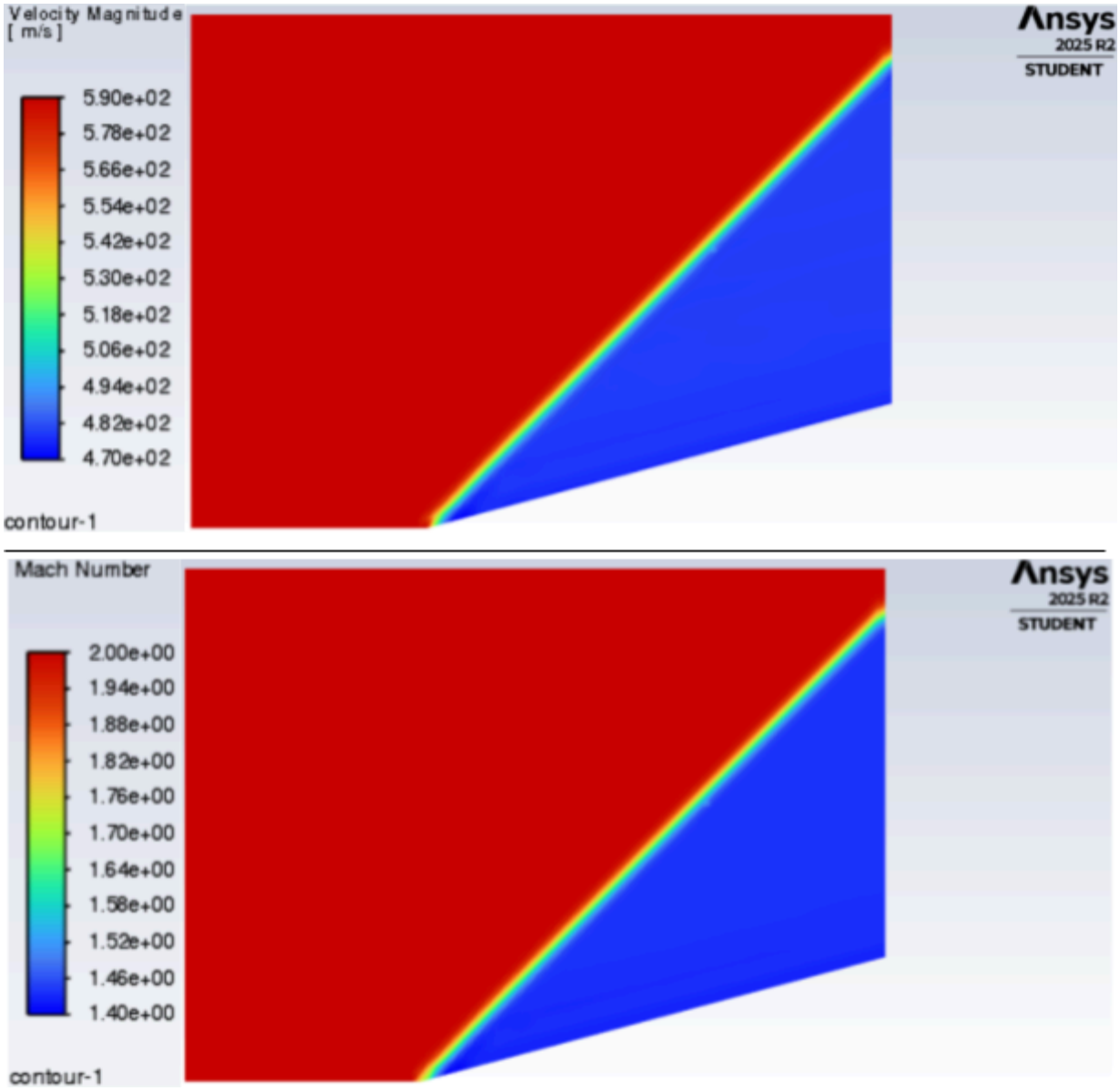


Figure 4.9 Velocity magnitude and Mach number contours (single wedge)

Figures 4.7-4.9 shows the contour fields for Mach number, static pressure, density, dynamic pressure, velocity magnitude, and static temperature in the single-wedge configuration. Together, these contours clearly show the production of an oblique shock anchored at the wedge's leading edge, with a significant increase in pressure, density, and temperature, as well as a matching decrease in the Mach number. Downstream of the shock, the contours become nearly uniform along the wedge surface, indicating a sustained, almost uniform flow after the shock. The combined set of contours shows in detail how the wedge geometry compresses and turns the supersonic freestream.

Table 4.1 shows the downstream values of the experimental 15^{o} wedge. As stated before the upstream values that are being used for the calculations for stagnation pressure and total

entropy are the same as the initial conditions from the upstream values seen in table 3.1 in chapter 3 values of Mach, pressure, density, velocity, dynamic pressure and temperature are approximated from the plots.

The two tables show that the stagnation pressure ratio and total entropy change tell slightly different stories about how the shock interaction was. The experimental values table 4.4, the stagnation pressure ratio from area 2 to region 1 is lower, while the total entropy rise is greater, indicating a stronger loss of total pressure and a more irreversible process across the shock. The theoretical Values in Table 3.1, the stagnation pressure ratio is higher while the entropy rise is notably lower, reflecting a weaker effective loss and a more efficient shock in thermodynamic terms. So, while the basic post-shock flow features are comparable, the first set of data represents a shock with more dissipation than the second.

Table 4.1 Experimental downstream values after shock at 15°

Definition	**Symbol**	**Value**	**Units**
Altitude	h	15,240	m
Gamma (Specific Heat Ratio)	γ	1.4	-
Gas Constant for Air	R	286	$\frac{J}{kg \cdot K}$
Speed of Sound	a2	331.2243952	$\frac{m}{s}$
Mach	M2	≈ 1.43	-
Velocity	V2	≈ 475	$\frac{m}{s}$
Temperature	T2	≈ 274	K
Pressure	P2	≈ 25,500	Pa
Density	ρ2	≈ 0.32	$\frac{kg}{m^3}$
Dynamic Pressure	q2	≈ 36,800	Pa
Stagnation Pressure Ratio from region 1 to 2	$\frac{P02}{P01}$	0.9268	-
Total Entropy from region 1 to 2	$\Delta S_{1\rightarrow2}$	21.74100112	$\frac{J}{kg \cdot K}$

4.4.2 Experimental results for 7.64° and 14.28° double wedge

For the double-wedge case, the residual trend demonstrates solid steady-state convergence, with some predicted oscillations due to the greater shock. The four equations of continuity, x-velocity, y-velocity, and energy begin near order 10^{0} and decrease rapidly over the first 300 to 350 iterations, passing through 10^{-2}, 10^{-3}, and settling near 10^{-4} to 10^{-5}. Around 150 to 250 iterations, there are a few abrupt spikes in the residuals as the solution adjusts to the evolving shock pattern over the two compression ramps, following which the residuals smooth out. Beyond around 400 iterations, the curves smooth out and exhibit small, periodic oscillations with about constant amplitude, which is typical of density-based supersonic flows in which one or more shocks travel slightly across a few cells as the solver progresses in a form of time. The lack of a long-term growth trend and the tight clustering of all four residuals imply that a statistically stable solution has been obtained, with the remaining variations attributed to shock interaction over the double-wedge geometry rather than global divergence. The residuals are shown in Figure 4.6.

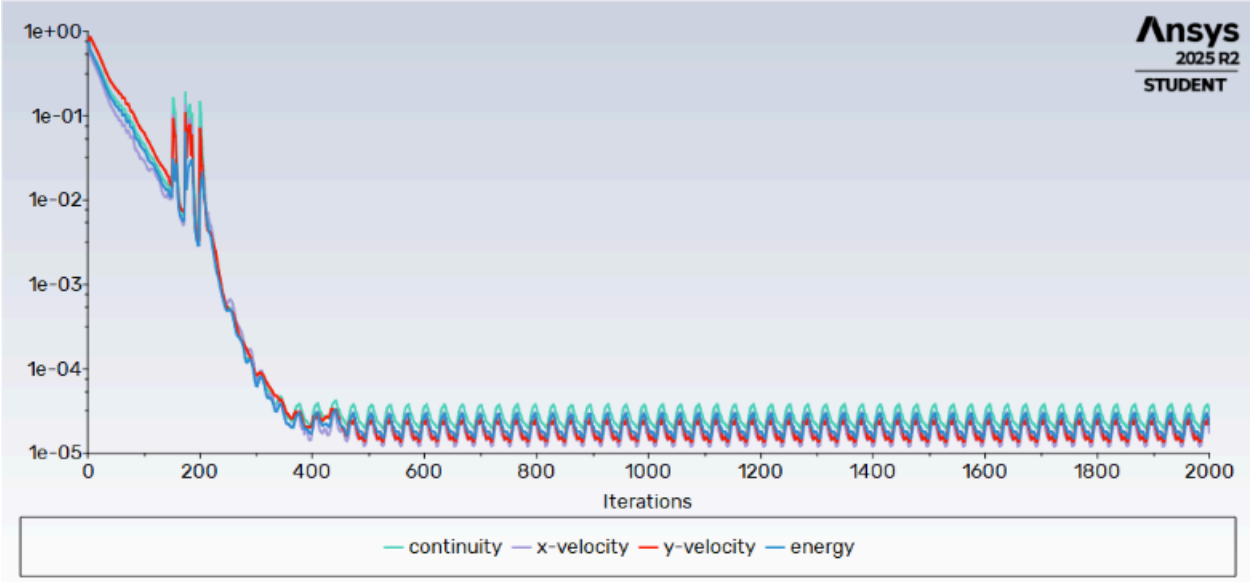


Figure 4.10 Residuals plot (double wedge)

The plots in figure 4.11 shows both the static pressure and dynamic pressure distribution along the surface

The static pressure distribution along the surface shows two step-like increases, which correspond to the two shocks produced by the double wedge. From the leading edge to the end of the first ramp, pressure rises from the freestream value to a slightly raised plateau, showing that the initial oblique shock is compressed only slightly. A sharper pressure jump occurs at the second corner, followed by a significant increase in static pressure over the second ramp and

trailing half of the wedge. The two-stage increase illustrates that the entire pressure rise is cumulative, with the second ramp generating the majority of the total compression.

The dynamic pressure distribution along the double wedge demonstrates the effect of the two shocks, however the changes are more subtle because they are dependent on both velocity and density. The dynamic pressure rises from its freestream level upstream of the first corner, forming a relatively uniform plateau along the first ramp that corresponds to the slight deceleration and density increase. At the second wedge angle, a visible change occurs, dynamic pressure reaches a local peak, followed by a new plateau at a slightly different level downstream. This trend reflects the competing impacts of further velocity reduction and increased density over the second shock, with the downstream region returning to a nearly uniform state once the flow has fully adjusted to the double-wedge shape.

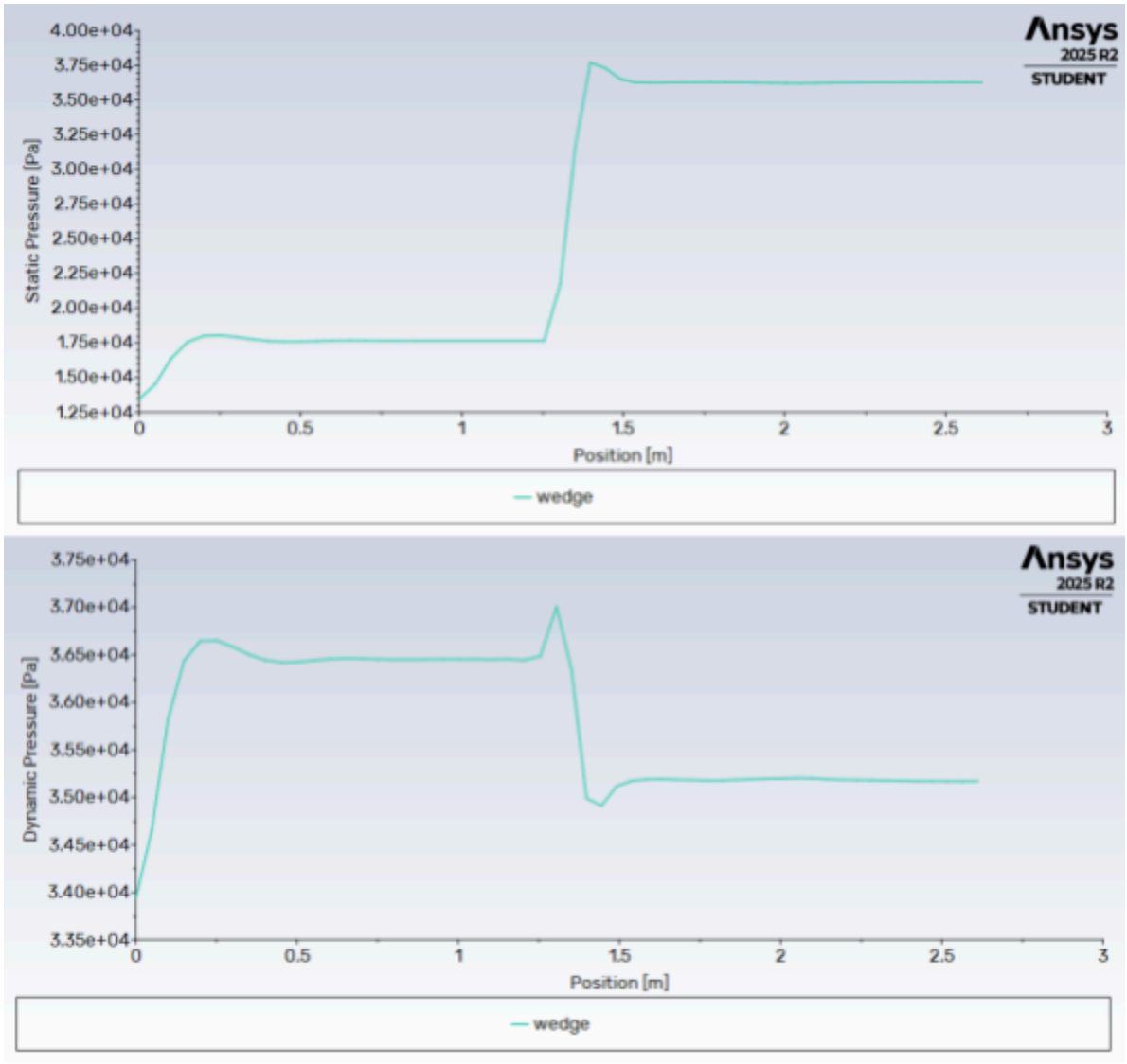


Figure 4.11 Static pressure and dynamic pressure plots (double wedge)

Figure 4.12 shows the plots of both the static temperature and density distribution across the double wedge configuration.

The static temperature distribution follows the opposite pattern as the Mach number, with two distinct jumps associated with the double-wedge geometry. Near the leading edge, the temperature is at freestream, then rises slightly across the first shock and forms a mild plateau along the first ramp. The second wedge corner shows a substantially larger rise in temperature, following which the curve levels off at a significantly higher value for the remainder of the length. This pattern shows the flow's cumulative compressive heating, a small temperature increase after the first deflection, followed by a bigger increase after the second, with the downstream plateau representing a virtually uniform high-temperature post-shock region.

The density distribution reflects the pressure behavior, with two distinct increases associated with double-wedge compression. Initially, the density is at freestream level, but then rises modestly across the first oblique shock, generating a fairly flat plateau on the first ramp. A larger increase in density appears at the second corner, followed by the curve flattening at a higher value over the remainder of the wedge. The appearance of these two plateaus separated by a steep second rise suggests that each ramp incrementally compresses the flow, with the second deflection causing the highest density of the supersonic stream.

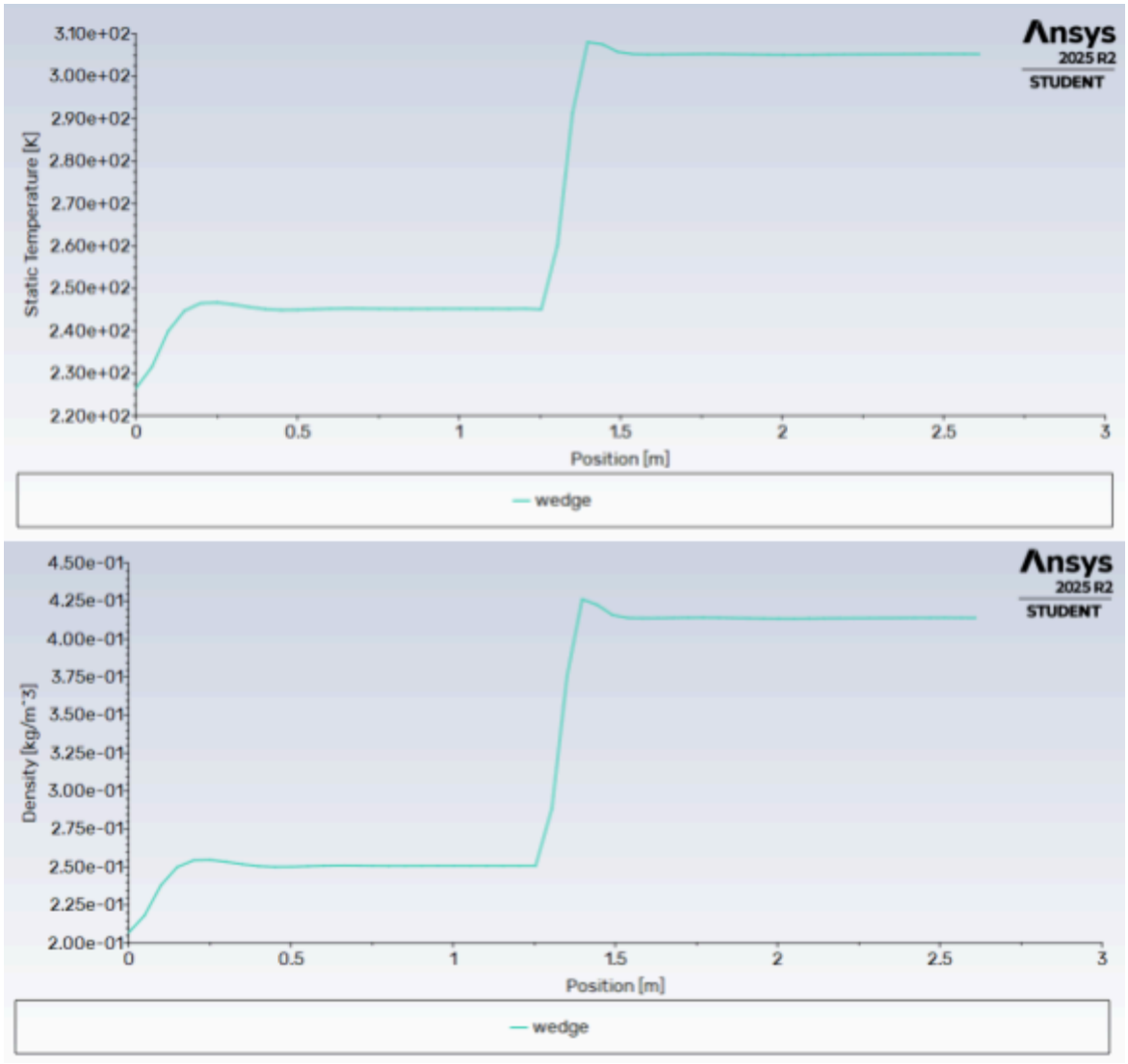


Figure 4.12 Static temperature and density plots (double wedge)

The plots in Figure 4.13 shows both the velocity magnitude and Mach distribution across the double wedge configuration.

The Mach number distribution across the double-wedge surface shows two separate compression events. Starting at the leading edge, the flow is at freestream Mach number and then drops to a little lower, but still clearly supersonic, level over the first ramp, showing a rather weak oblique shock associated with the initial wedge angle. The Mach number then maintains practically constant along the first plateau region until it reaches the second corner, when it drops dramatically as the flow is turned over the second wedge. Downstream of this second discontinuity, the Mach number settles to a lower, virtually uniform value, indicating that the second ramp causes the major fall in Mach number and sets the final post-shock state across the wedge's rear part.

The velocity magnitude plot shows the projected decline of the flow as it passes through two consecutive shocks. The curve begins at a high freestream velocity near the leading edge, gradually decreases throughout the first shock, and then remains almost constant down the first ramp. When the flow approaches the second wedge angle, velocity decreases more dramatically, lowering the value to a lower plateau that spans over the back portion of the surface. This two-step reduction demonstrates how the double-wedge geometry gradually slows the flow, a modest deceleration over the first ramp, followed by a sharper slowdown as the flow turns more at the second corner.

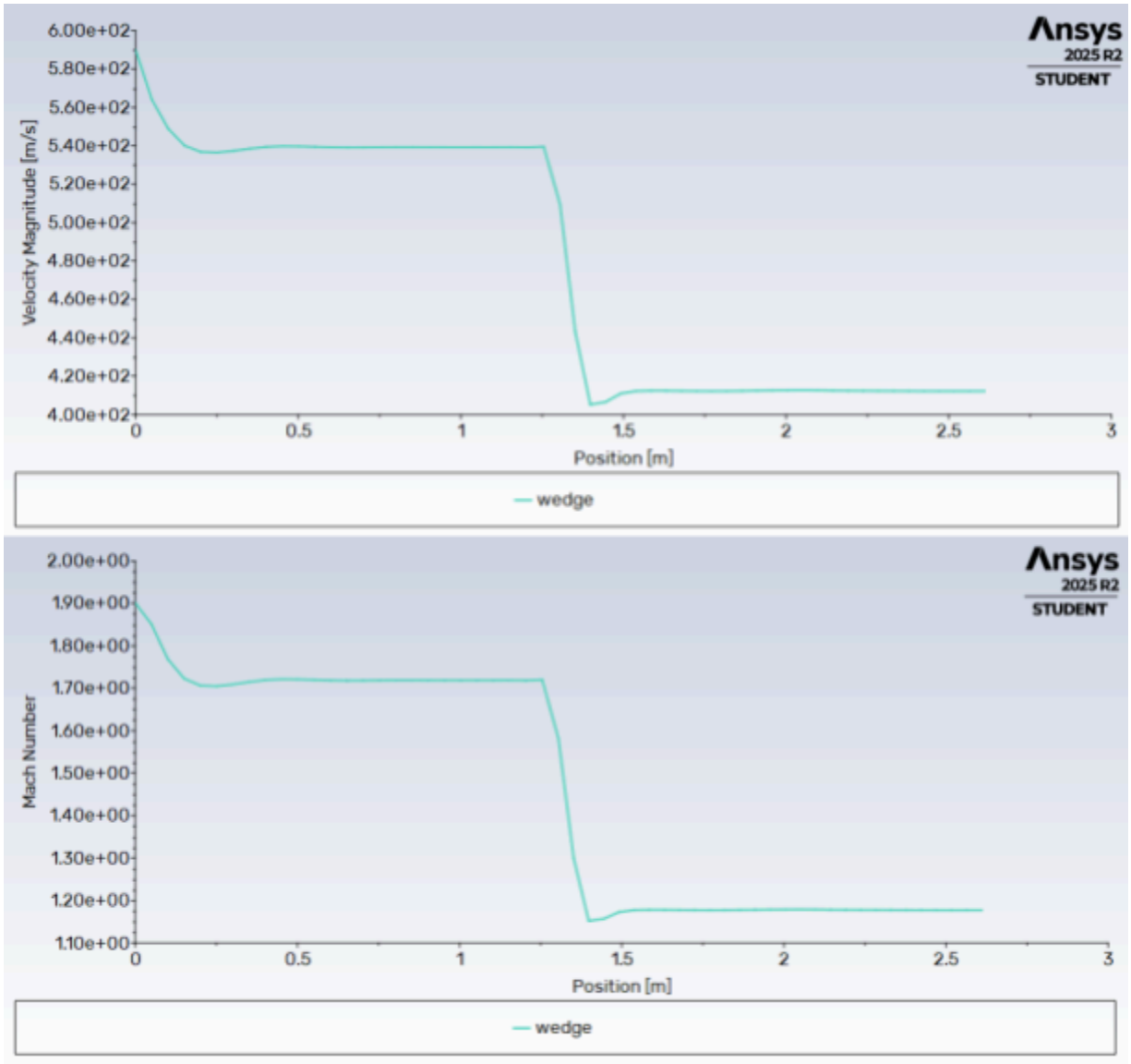


Figure 4.13 Velocity magnitude and Mach plots (double wedge)

Figures 4.14-4.16 shows the contour fields for Mach number, static pressure, density, dynamic pressure, velocity magnitude, and static temperature in a double-wedge configuration.

In contrast to the single-wedge case, the contours now reveal a two-shock system, with an initial oblique shock anchored at the first ramp and a second, greater shock generated at the downstream ramp. Pressure, density, and temperature rise in two stages across these shocks, while Mach number and velocity fall, with the largest increases occurring at the second deflection. The contours form discrete plateau zones between the shocks and across each ramp, showing quasi-uniform intermediate and final post-shock conditions.

Taken together, the contour graphs show how the double-wedge shape compresses and turns the supersonic freestream, resulting in a lower-Mach, higher-pressure flow over the second ramp.

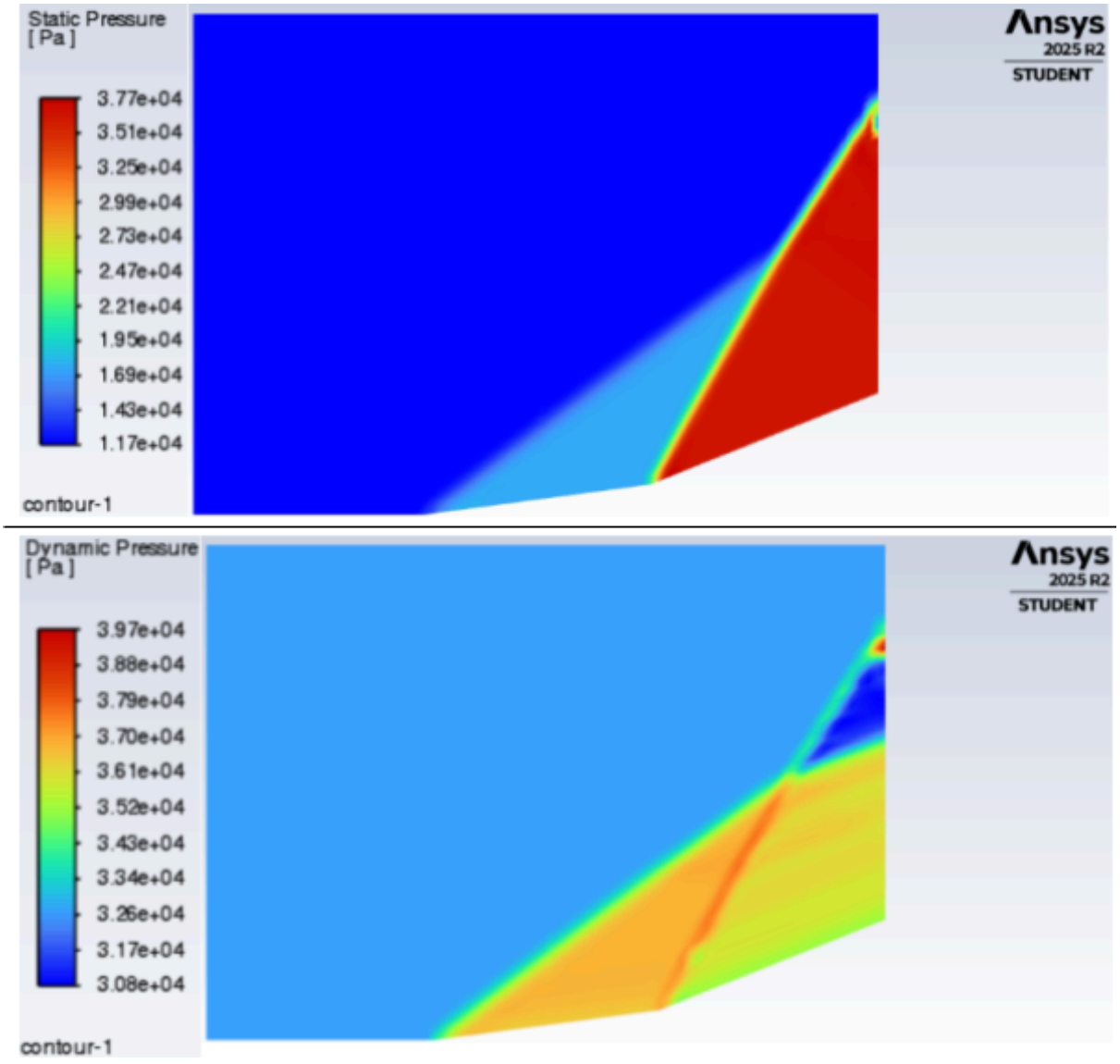


Figure 4.14 Static pressure and dynamic pressure contours (double wedge)

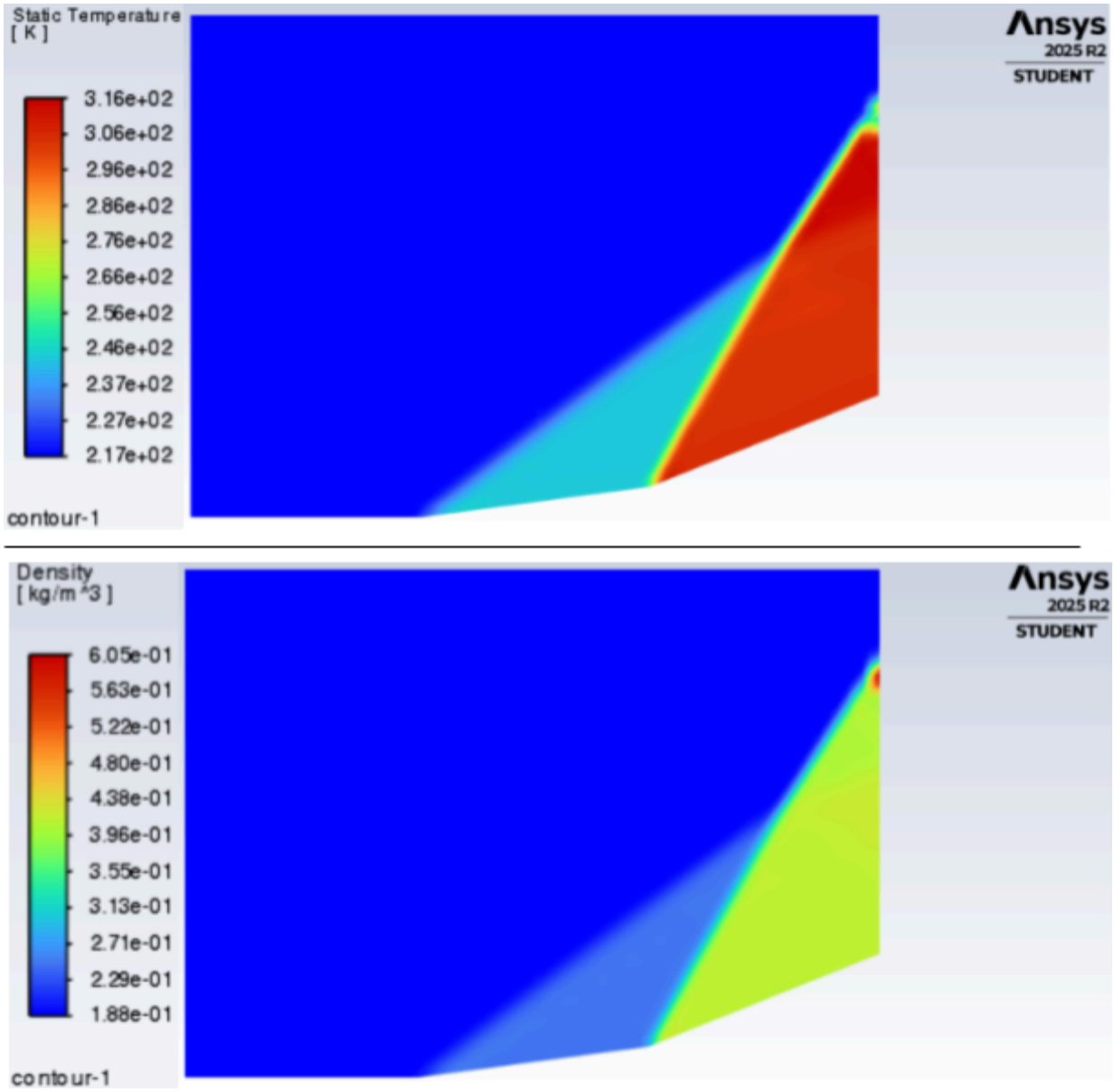


Figure 4.15 Static temperature and density contours (double wedge)

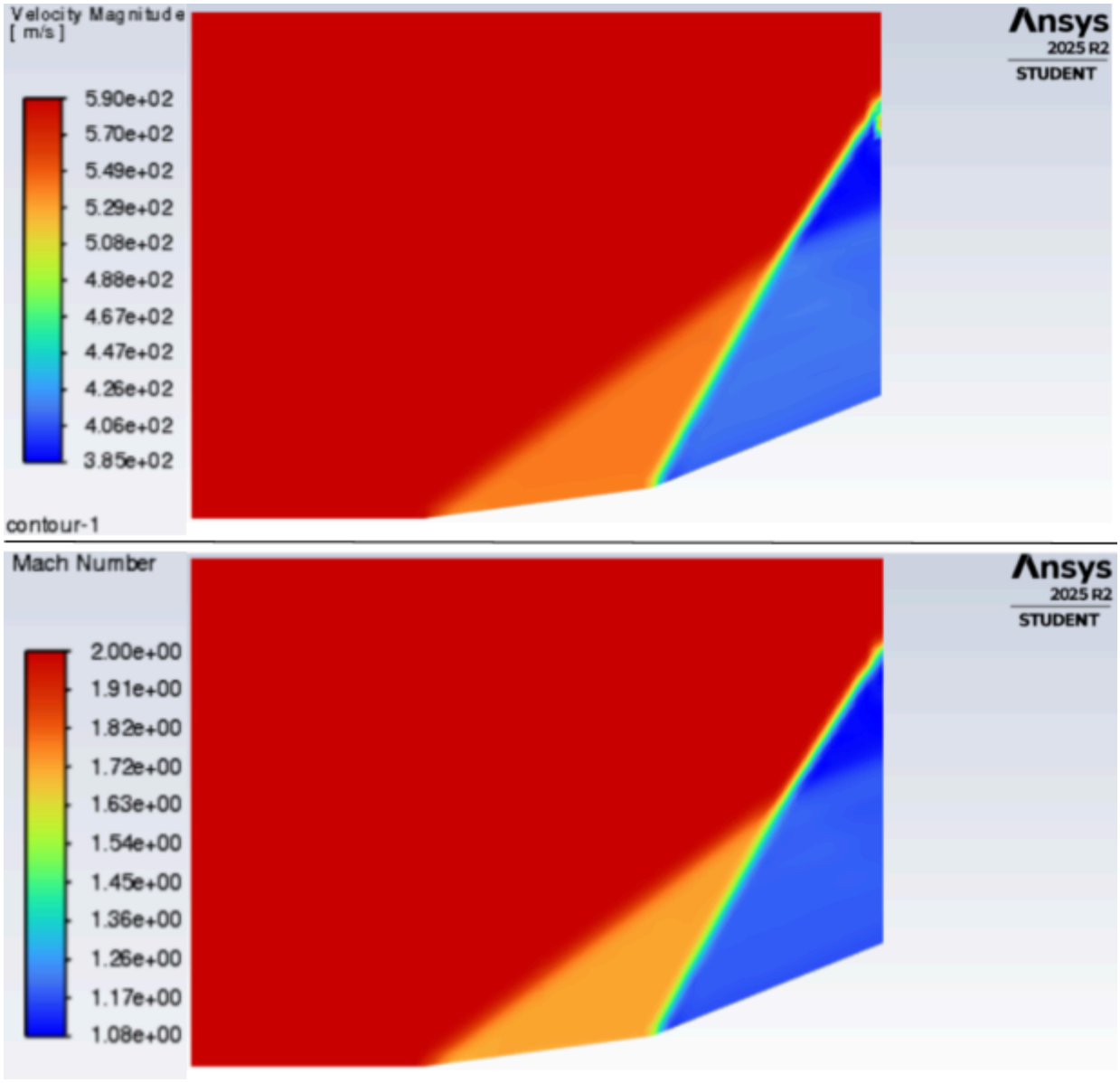


Figure 4.16 Velocity magnitude and Mach contours (double wedge)

The same way values of Mach, pressure, density, velocity, dynamic pressure and temperature were approximated in Table 4.1 downstream of the single shock, Downstream Values of the double wedge will also be approximated and compared to the same initial values in table 3.1. Table 4.2 and 4.3 shows the experimental downstream values of the flow of both shock interactions at 7.64º and 14.28º.

The theoretical double-wedge results in Tables 3.3 and 3.4 show the ideal post-shock states for each ramp, and the experimental values nearly match them. At 7.64º, the experimental Mach number, velocity, pressure, density, dynamic pressure, and temperature almost exactly match the theoretical trends. The flow remains clearly supersonic, the velocity reduction is minimal, and the increases in pressure, density, and temperature are small, as expected for a

relatively weak first shock. Any discrepancies are small and primarily due to rounding and the fact that the CFD values were obtained from a finite, somewhat smeared plateau rather than a perfect discontinuity.

At 14.28°, the contrast is equally good. Both theoretical and experimental states show a stronger second compression, Mach number and velocity fall further, while pressure, density, and temperature rise more noticeably than they did over the first ramp. The observed plateau values closely match the theoretical values, with only minor differences due to numerical dissipation and mesh resolution. Overall, the experimental double-wedge data support the theoretical predictions in Tables 3.3 and 3.4, accurately capturing both the relative strength of the two shocks and the amplitude of the downstream flow features.

Table 4.2 Experimental downstream values after shock at 7.64°

Definition	**Symbol**	**Value**	**Units**
Altitude	h	15,240	m
Gamma (Specific Heat Ratio)	γ	1.4	-
Gas Constant for Air	R	286	$\frac{J}{kg \cdot K}$
Speed of Sound	a2	313.2060025	$\frac{m}{s}$
Mach	M2	≈ 1.72	-
Velocity	V2	≈ 540	$\frac{m}{s}$
Temperature	T2	≈ 245	K
Pressure	P2	≈ 17,500	Pa
Density	ρ2	≈ 0.25	$\frac{kg}{m^3}$
Dynamic Pressure	q2	≈ 36,500	Pa
Stagnation Pressure Ratio from region 1 to 2	$\frac{P02}{P01}$	0.974562	-
Total Entropy from region 1 to 2	$\Delta S_{1\rightarrow 2}$	7.369385	$\frac{J}{kg \cdot K}$

Table 4.3 Experimental downstream values after shock at 14.28°

Definition	Symbol	Value	Units
Altitude	h	15,240	m
Gamma (Specific Heat Ratio)	γ	1.4	-
Gas Constant for Air	R	286	$\frac{J}{kg \cdot K}$
Speed of Sound	a3	349.4595828	$\frac{m}{s}$
Mach	M3	1.2	-
Velocity	V3	415	$\frac{m}{s}$
Temperature	T3	305	K
Pressure	P3	36000	Pa
Density	ρ3	0.41	$\frac{kg}{m^3}$
Dynamic Pressure	q3	36000	Pa
Stagnation Pressure Ratio from region 2 to 3	$\frac{P03}{P02}$	0.9806	-
Stagnation Pressure Ratio from region 1 to 3	$\frac{P03}{P01}$	0.955618	-
Total Entropy from region 2 to 3	$\Delta S_{2\rightarrow3}$	5.602925833	$\frac{J}{kg \cdot K}$
Total Entropy from region 1 to 3	$\Delta S_{1\rightarrow3}$	12.98354983	$\frac{J}{kg \cdot K}$

4.5 Entropy Change and Stagnation Pressure Ratio of Experimental Wedges

Table 3.5 shows the experimental values of single-wedge and double wedge total pressure and change in entropy. The single wedge generates a fairly large oblique shock, results in a significant drop in stagnation pressure and a huge increase in entropy. This points to a highly

irreversible compression process with large total-pressure losses when the flow travels through the single, steep curve.

The double-wedge arrangement, in comparison, divides the entire flow deflection into two smaller shocks. The observed results indicate that, while entropy increases and stagnation pressure decreases, the losses are fewer than in the single-wedge scenario. In thermodynamic words, the double-wedge compression is less irreversible, the flow retains more of its upstream stagnation pressure and sees a smaller entropy rise as it navigates the two-stage turn.

In total comparison, these findings indicate that, under the experimental conditions studied, the double-wedge design is closer to the ideal isentropic limit than the single-wedge design. It achieves the desired overall flow turning while causing less total-pressure loss and entropy rise, making it the more efficient configuration in terms of compressible flow.

Table 4.4 Comparison of experimental total stagnation pressure and entropy in the single and double wedge configurations

Configuration	**Angle in Degrees**	**Stagnation Pressure across System (Total Pressure)**	**Entropy of System**
Single Wedge	15^{o}	$\frac{P02}{P01} = 0.9268$	$\Delta S_{1\rightarrow 2} = 21.74100112$
Double Wedge	7.64^{o} and 14.28^{o}	$\frac{P03}{P01} = 0.955618$	$\Delta S_{1\rightarrow 3} = 12.98354983$
Percent Change		+3.1094%	-40.28%

5 Entropy and Stagnation Pressure: Theoretical vs Experimental Percent Error

5.1 Overview

This chapter compares theoretical and experimental data for stagnation pressure and entropy in both single- and double-wedge designs. Using the stagnation pressure ratios and entropy changes presented in Table 5.1, the chapter calculates percent errors for each scenario and assesses how well the CFD findings match the oblique-shock theory. The disparities are analyzed in terms of shock strength, total-pressure loss, and irreversibility, with a focus on which configuration is thermodynamically closest to the ideal isentropic limit and the numerical or physical reasons may explain the remaining differences.

5.2 Percent Error and Comparisons

Table 5.1 compares theoretical and experimental stagnation pressure ratios, as well as entropy changes, for the single-wedge at 15^{o} and double-wedge configurations at 7.64^{o} and 14.28^{o}. For stagnation pressure, both cases show very good agreement with theory, the single wedge has a theoretical ratio of about 0.952 and an experimental value of 0.927, giving a small error of about 2.7%, whereas the double wedge shows almost perfect agreement, with essentially the same theoretical and experimental ratios and negligible errors. This suggests that the CFD/experimental configuration accurately captures the overall shock strength and total pressure loss, especially for the double wedge.

The entropy comparison shows larger changes, but it maintains the same physical tendencies. The theoretical entropy increase for the double wedge is smaller than for the single wedge, and the experimental results support this ordering. However, the experimental entropy changes are significantly larger than the theoretical predictions, notably for the single wedge, which has an inaccuracy of around 56%, compared to roughly 28% for the double wedge.

This suggests that entropy is far more prone to numerical and post-processing variables than the stagnation pressure ratio. This could come from plateau value selection, shock smearing, and local gradients. Overall, the table demonstrates that the double-wedge configuration not only corresponds more closely with theory, but it is also thermodynamically closer to the ideal prediction, whereas the single wedge shows greater irreversibility and entropy estimate differences.

Table 5.1 Theoretical vs experimental percent error

Configuration	$P0_{downstream}/P01$ (Theoretical)	$P0_{downstream}/P01$ (Experimental)	% Error (P0)	Entropy (Theoretical) (ΔS)	Entropy (Experimental) (ΔS)	% Error (ΔS)
Single Wedge (15^{o})	0.952356	0.9268	2.6835	13.96148025	21.74100112	55.72

Double Wedge (7.64^o and 14.28^o)	0.956113	0.955618	0.05177	10.15588461	12.98354983	27.84
Units	-	-	-	$\frac{J}{kg \cdot K}$	$\frac{J}{kg \cdot K}$	-

6 Comprehensive Discussion

Throughout this study, supersonic flow across single and double-wedge geometries were analyzed using analytical oblique-shock relations and CFD simulations to measure total-pressure loss and entropy production. The fundamental question was whether breaking the overall flow deflection into two smaller shocks, corresponding to a double-wedge nose, provided a thermodynamic advantage over a single stronger wedge at the same freestream Mach number. The combined theoretical MATLAB calculations and CFD experimental results provide an accurate conclusion, both approaches suggest that the double-wedge structure has lower losses and is more efficient from a compressible-flow perspective.

The theoretical analysis gathered from MATLAB provided a precise basis for comparison. Using traditional theta-beta-Mach and normal-shock equations, the single 15^{o} wedge was demonstrated to generate a relatively powerful oblique shock, with a notable reduction in stagnation pressure and a higher increase in entropy across the system. In comparison, the double-wedge structure with deflections of 7.64^{o} and 14.28^{o} produced two progressively smaller shocks that combined to achieve the same overall turning with a little greater stagnation-pressure ratio and a somewhat lower total rise in entropy. These theoretical trends have already indicated that distributing compression across numerous ramps brings the system closer to the ideal isentropic limit.

The CFD results provided an independent numerical experiment to validate these predictions. Surface distributions and flowfield contours of both the single and double wedges revealed the expected step shifts at the shock locations. Mach number and velocity decreased, but static pressure, density, temperature, and dynamic pressure increased to new, relatively uniform plateaus downstream. In the double-wedge case, all properties showed two distinct discontinuities, corresponding to the two shocks, with the second shock causing the biggest thermodynamic jump. The derived downstream states from these plateaus nearly matched the predicted values for Mach number, velocity, temperature, and pressures at each wedge angle, indicating that the ANSYS Fluent setup and meshing method were adequate for capturing the crucial oblique-shock behavior.

When the theoretical results were directly compared to CFD results based on stagnation-pressure ratios and entropy changes, the disparities were clear. For stagnation pressure, both wedges matched the theory quite well, the single wedge was off by only a few percentage points, while the double wedge was nearly identical to the theoretical value. This demonstrates that the CFD model accurately predicts the amount of total pressure lost due to shocks. However, entropy did not match quite as well. The single wedge deviated the most from theory, while the double wedge maintained the same pattern but with a lesser separation. This implies that entropy is far more sensitive to numerical parameters in the simulation, such as how the shock is distributed across multiple cells and how the downstream plateau values are set.

7 Conclusion and Future Work

Overall, both theory and CFD indicate the same physical result, the double wedge is more efficient than the single wedge under the conditions investigated. Splitting the flow into two smaller shocks minimizes irreversibility, retains more stagnation pressure, and limits the increase in entropy while maintaining the same total deflection. Despite the study's limitation to a 2D, inviscid model at one Mach number, the match between the approaches indicates a credible trend. Multi-ramp compression surfaces, such as a double-wedge nose or an external compression inlet, can provide significant advantages over a single sharp bend in supersonic flow.

Three key future improvements stand out for expanding this study. The first step is to investigate increasingly complex multi-wedge geometries. The current study solely compares a single 15^{o} wedge to two-ramp configurations with 7.64^{o} and 14.28^{o} deflections. A reasonable next step would be to divide the original wedge into three or more smaller ramps and gradually adjust the individual angles. This would allow us to observe how stagnation-pressure loss and entropy generation changes as compression is distributed over a larger number of lesser shocks. With a larger sample size, patterns might be identified and ideal angle combinations could be presented to minimize losses for a given overall flow deflection.

The second major step is to fine-tune the mesh in and around the shock zones. In the current simulations, the grid is fine enough to catch the primary oblique shocks and downstream plateaus, but the shocks are still dispersed across several cells, affecting the accuracy of entropy estimates. Future research should include local mesh refining at the expected shock areas, either through biasing or adaptive refinement, and then repeat the calculations as part of a structured grid-convergence study. Comparing stagnation-pressure ratios and entropy changes across multiple mesh levels would help distinguish true physical trends from numerical dissipation, as well as determine how much additional resolution is required to accurately resolve shock thickness and post-shock gradients in these wedge configurations [16, 17].

The third consideration is to look beyond the inviscid flow assumption and incorporate viscous and turbulent models. The current analysis ignores boundary layers and shock-boundary-layer interactions, which might cause significant total-pressure loss and entropy generation in real flows. To quantify the influence of viscosity and turbulence on stagnation-pressure loss and entropy generation, using a suitable turbulence model (for example, k-ω SST model) with wall effects. Combining this with mesh refinement at the wall and in the shock region would bring the simulations closer to real-world aerodynamic circumstances and determine if the relative advantage of multi-wedge geometries is as high when viscous effects are considered.

References

[1] Wolff, M., Abada, H. H., Saad, H. A. K. “Numerical Investigation of Supersonic Flow over a Wedge by Solving 2D Euler Equations Utilizing the Steger–Warming Flux Vector Splitting (FVS) Scheme.” *Mathematics*, Vol. 12, No. 9, p. 1282., April. 2024. https://doi.org/10.3390/math12091282.

[2] Ray, A. A., & De, A. “Investigation of turbulent high-speed flow over the double wedge at varying aft-wedge deflections,” *European Journal of Mechanics / B Fluids*, *111*, pp. 20-41., June. 2025. https://doi.org/10.1016/j.euromechflu.2024.11.012

[3] Xie, W., Luo Z., Wang, H., and Liu, Q., Zhou, Y. “Experimental Study on Unsteadiness in the Double Wedge Type-V Shock/Shock Interaction with Varying Second-Wedge Angles.” *Experimental Thermal and Fluid Science*, Vol. 170, p. 111574., January. 2026. https://doi.org/10.1016/j.expthermflusci.2025.111574.

[4] Slater, J. W., “Off-Design Analysis of Axisymmetric External-Compression Supersonic Inlets for Mach 1.4 to 2.0,” Paper ISABE-2024-022, *ISABE 2024.*, June. 2024. https://ntrs.nasa.gov/citations/20240007797

[5] Bachman, C. L., and Goodwin, G. B. “Ignition Criteria and the Effect of Boundary Layers on Wedge-Stabilized Oblique Detonation Waves.” *Combustion and Flame*, Vol. 223, pp. 271-283., January. 2021. https://doi.org/10.1016/j.combustflame.2020.10.007.

[6] Anderson, J. D., “Modern Compressible Flow: With Historical Perspective”, McGraw Hill., 2003.

[7] Ezzeldin, A., and Wu, Z., “CFD-Driven Enhancement for Supersonic Aircraft Variable Geometry Inlet,” *Applied Sciences*, Vol. 15, No. 17, Art. No. 9825., September. 2025. https://www.mdpi.com/2076-3417/15/17/9825

[8] Varma, A. S., Sathyanarayana, G. S., and Sandeep, J., “CFD Analysis of Various Nose Profiles,” *International Journal of Aerospace and Mechanical Engineering*, Vol. 3, No. 3, pp. 26-29., June. 2016. https://www.scribd.com/document/942043012/CFD-Analysis-of-Various-Nose-Profiles

[9] Mason, M. L., “Experimental Investigation of Shock-Shock Interactions Over a 2D Wedge at M = 6,” NASA/TP-20205011524, National Aeronautics and Space Administration., December 2020. https://ntrs.nasa.gov/citations/20205011524

[10] NASA Glenn Research Center, “Earth Atmosphere Model - Metric Units,” Glenn Research Center., May. 2021. https://www.grc.nasa.gov/www/k-12/airplane/atmosmet.html

[11] NASA Glenn Research Center, “Speed of Sound,” NASA Glenn Research Center (K-12 Aeronautics). https://www.grc.nasa.gov/www/k-12/VirtualAero/BottleRocket/airplane/sound.html.

[12] NASA Glenn Research Center, “Mach Number,” NASA Glenn Research Center., May. 2021. https://www.grc.nasa.gov/www/k-12/airplane/mach.html

[13] U.S. Air Force, “F-16 Fighting Falcon,” U.S. Air Force Official Website., September. 2021. https://www.af.mil/About-Us/Fact-Sheets/Display/Article/104505/f-16-fighting-falcon/

[14] Virginia Tech — Dept. of Aerospace and Ocean Engineering, *AOE3114 Calculations Page.,* December. 2023. https://devenport.aoe.vt.edu/aoe3114/calc.html.

[15] ANSYS, “Supersonic Flow Over a Wedge: Ansys Solution Outline (Pre-analysis),” ANSYS Innovation Space (course material). https://innovationspace.ansys.com/courses/wp-content/uploads/sites/5/2024/09/wedge_solution_outline.pdf

[16] Duan, R., Liu, W., Xu, L., Huang, Y., Shen, X., Lin, C.-H., Liu, J., Chen, Q., and Sasanapuri, B., “Mesh Type and Number for the CFD Simulations of Air Distribution in an Aircraft Cabin,” *Numerical Heat Transfer, Part B: Fundamentals*, Vol. 67, No. 6, pp. 489-506., April. 2015. https://www.researchgate.net/publication/274514708_Mesh_Type_and_Number_for_the_CFD_Simulations_of_Air_Distribution_in_an_Aircraft_Cabin

[17] Coder, J. G., Couchman, B. L. S., Galbraith, M. C., Allmaras, S. R., and Wyman, N., “Output-Based Mesh Adaptation for High-Speed Flows,” *Computers & Fluids*, Vol. 273, Art. No. 106208., April. 2024. https://www.sciencedirect.com/science/article/abs/pii/S0045793024000409

[18] Piccirillo, A. C., “Elegance in Flight: A Comprehensive History of the F-16XL Experimental Prototype and its Role in NASA Flight Research,” NASA SP-2014-618, National Aeronautics and Space Administration, Washington, D.C., 2014. https://www.nasa.gov/aeronautics/elegance-in-flight/

[19] Public Intelligence, “Flight Manual HAF Series Aircraft F16C/D,” Lockheed Martin Corporation., June. 2003. https://info.publicintelligence.net/HAF-F16.pdf.

Appendix A: Matlab Script for Theoretical Oblique Shock over a Supersonic Aircraft Nose (1 Wedge)

```
%  Theoretical Oblique Shock over a Supersonic Aircraft Nose (1 Wedge)
%  Region 1: Freestream at h1 = 50,000 ft (15,240 m), M1 = 2.0
%  Region 2: Downstream of single oblique shock (theta = 15 deg)
%  Assumptions:
%   - Steady, adiabatic, calorically perfect gas
%   - No shaft work
%   - Atmosphere from NASA Earth Atmosphere Model (11 km < h < 25 km)

clear; clc;

% Gas Properties for Air
gamma = 1.4;                % Ratio of specific heats for air
R     = 286;                % Gas constant for air (J/(kg*K))

%% Region 1 Freestream Values
% Flight Condition
h1 = 15240;                 % Altitude (m) (50,000 ft)
M1 = 2.0;                   % Upstream Mach number

% NASA Atmosphere model at Lower Stratosphere (11 km < h < 25 km)
T1_C = -56.46;                              % Temperature (°C)
T1 = T1_C + 273.15;                         % Temperature (K)
P1_kPa = 22.65 * exp(1.73 - 0.000157*h1);   % Pressure (kPa)
P1 = P1_kPa * 1e3;                          % Pressure (Pa)


% Thermodynamic Flow properties
rho1 = P1 / (R * T1);                       % Density (kg/m^3)
a1 = sqrt(gamma * R * T1);                  % Speed of Sound (m/s)
V1 = M1 * a1;                               % Velocity (m/s)

% Wedge Deflection Angle (geometry)
theta_deg = 15.0;                           % Wedge Deflection (deg)

%% Shock from Region 1 to Region 2
theta = theta_deg * pi/180;                 % Deflection angle (rad)

% Theta-Beta-Mach relation for Region 1
thetaBetaM = @(beta) atan( ...
   2 * (cos(beta)./sin(beta)) .* (M1^2 .* sin(beta).^2 - 1) ./ ...
   (M1^2 .* (gamma + cos(2*beta)) + 2) );

% Solve thetaBetaM(beta) = theta (weak shock solution)
beta_in_deg =  45.3436167;                      % Calculated Beta (deg)
beta_in_rad = beta_in_deg * pi/180;             % Converting (rad)
f_beta = @(beta) thetaBetaM(beta) - theta;
beta = fzero(f_beta, beta_in_rad);              % Shock Angle (rad)

% Normal Mach number Upstream
Mn1 = M1 * sin(beta);
```

```
% Normal Shock relation (Region 1 to Region 2)
rho2_rho1 = ((gamma + 1)*Mn1^2) / (2 + (gamma - 1)*Mn1^2);
p2_p1     = 1 + (2*gamma/(gamma + 1))*(Mn1^2 - 1);
T2_T1     = p2_p1 / rho2_rho1;

% Normal Mach Downstream
Mn2_sq = (1 + 0.5*(gamma - 1)*Mn1^2) / ...
        (gamma*Mn1^2 - 0.5*(gamma - 1));
Mn2 = sqrt(Mn2_sq);

% Downstream Mach Number in Region 2
M2 = Mn2 / sin(beta - theta);

% Region 2 static properties (Temperature, Pressure, and Density)
T2   = T1   * T2_T1;
P2   = P1   * p2_p1;
rho2 = rho1 * rho2_rho1;

% Region 2 Speed of Sound and Velocity
a2 = sqrt(gamma * R * T2);
V2 = M2 * a2;

% Dynamic Pressures in Region 1 and Region 2
q1 = 0.5 * rho1 * V1^2;
q2 = 0.5 * rho2 * V2^2;

% Stagnation Pressure Ratios  in Region 1 and Region 2
% Total Stagnation Pressures in each Region
P01 = P1 * (1 + (gamma - 1)/2 * M1^2)^(gamma/(gamma - 1));
P02 = P2 * (1 + (gamma - 1)/2 * M2^2)^(gamma/(gamma - 1));
%  Ratios across Shock Wave
P02_P01 = P02 / P01;   % 1st shock (theta1)

% Printing Results
fprintf('Region 1 (Upstream Values at h = 50,000 ft / 15,240 m)\n');
fprintf('M1 = %.6f\n', M1);
fprintf('T1 = %.6f K\n', T1);
fprintf('P1 = %.6f Pa\n', P1);
fprintf('rho1 = %.6f kg/m^3\n', rho1);
fprintf('a1 = %.6f m/s\n', a1);
fprintf('V1 = %.6f m/s\n', V1);
fprintf('q1 = %.6f Pa\n\n', q1);
fprintf('Region 2 (Region 1 to Region 2 Downstream)\n');
fprintf('M2 = %.6f\n', M2);
fprintf('T2 = %.6f K\n', T2);
fprintf('P2 = %.6f Pa\n', P2);
fprintf('rho2 = %.6f kg/m^3\n', rho2);
fprintf('a2 = %.6f m/s\n', a2);
fprintf('V2 = %.6f m/s\n', V2);
fprintf('q2 = %.6f Pa\n', q2);
fprintf('\nStagnation Pressure Ratios\n');
fprintf('P02/P01 = %.6f\n', P02_P01);

%% Graphs with respect to position (Mach, Temperature, Static Pressure, Velocity,
Density, and Dynamic Pressure)
```

```
% Position along the nose and flow direction
x_start = -1;             % 1m upstream of the nose
x_end = 3;                % 3m downstream
Nx = 500;
x = linspace(x_start, x_end, Nx);

% Shock locations along x-Position
x_shock = 0.0;          % shock at nose

% Preallocate arrays for all properties vs x (Position)
M_x = zeros(size(x));   % Mach 1
T_x = zeros(size(x));   % Temperature 1 (K)
P_x = zeros(size(x));   % Pressure 1 (kPa)
rho_x = zeros(size(x)); % Density 1 (kPa)
V_x = zeros(size(x));   % Velocity 1 (m/s)
q_x = zeros(size(x));   % Dynamic Pressure 1 (kPa)

% Indices for each region
idx1 = x <  x_shock;    % Region 1
idx2 = x >= x_shock;    % Region 2

% Region 1 Upstream Values
M_x(idx1) = M1;
T_x(idx1) = T1;
P_x(idx1) = P1;
rho_x(idx1) = rho1;
V_x(idx1) = V1;
q_x(idx1) = q1;


% Region 2 Downstream of 1st Shock Values
M_x(idx2) = M2;
T_x(idx2) = T2;
P_x(idx2) = P2;
rho_x(idx2) = rho2;
V_x(idx2) = V2;
q_x(idx2) = q2;

% Plotting Sections
figure;
subplot(3,2,1);
plot(x, M_x, 'LineWidth', 2);
hold on;
xline(x_shock, '--');
grid on;
xlabel('x-position(m)');
ylabel('M');
title('Mach Number v. Position');
legend('M(x)', 'Shock', 'Location', 'best');
subplot(3,2,2);
plot(x, T_x, 'LineWidth', 2);
hold on;
xline(x_shock, '--');
grid on;
xlabel('x-position(m)');
```

```
ylabel('T (K)');
title('Temperature v. Position');
legend('T(x)', 'Shock', 'Location', 'best');
subplot(3,2,3);
plot(x, P_x/1e3, 'LineWidth', 2);
hold on;
xline(x_shock, '--');
grid on;
xlabel('x-position(m)');
ylabel('P (kPa)');
title('Static Pressure v. Position');
legend('P(x)', 'Shock', 'Location', 'best');
subplot(3,2,4);
plot(x, V_x, 'LineWidth', 2);
hold on;
xline(x_shock, '--');
grid on;
xlabel('x-position(m)');
ylabel('V (m/s)');
title('Velocity v. Position');
legend('V(x)', 'Shock', 'Location', 'best');
subplot(3,2,5);
plot(x, rho_x, 'LineWidth', 2);
hold on;
xline(x_shock, '--');
grid on;
xlabel('x-position(m)');
ylabel('\rho (kg/m^3)');
title('Density v. Position');
legend('rho(x)', 'Shock', 'Location', 'best');
subplot(3,2,6);
plot(x, q_x/1e3, 'LineWidth', 2);
hold on;
xline(x_shock, '--');
grid on;
xlabel('x-position(m)');
ylabel('q (kPa)');
title('Dynamic Pressure v. Position');
legend('q(x)', 'Shock', 'Location', 'best');
```

Appendix B: Matlab Script for Theoretical Oblique Shock over a Supersonic Aircraft Nose Double Wedge (2 Wedge)

```
%  Theoretical Oblique Shock Calculations over a Supersonic Aircraft Nose 2 Wedges
%  Region 1: Freestream at h1 = 50,000 ft (15,240 m), M1 = 2.0
%  Region 2: Downstream of 1st oblique shock (theta1 = 7.64 deg)
%  Region 3: Downstream of 2nd oblique shock (theta2 = 14.28 deg)
%  Assumptions:
%   - Steady, adiabatic, calorically perfect gas
%   - No shaft work
%   - Atmosphere from NASA Earth Atmosphere Model (11 km < h < 25 km)

clear; clc;

% Gas Properties for Air
gamma = 1.4;                % Ratio of specific heats for air
R = 286;                    % Gas constant for air (J/(kg*K))

% Region 1 Freestream Values
% Flight Condition
h1 = 15240;                 % Altitude in meters (50,000 ft)
M1 = 2.0;                   % Upstream Mach number

% NASA Atmosphere model at Lower Stratosphere (11 km < h < 25 km)
T1_C = -56.46;                               % Temperature (°C)
T1 = T1_C + 273.15;                          % Temperature (K)
P1_in_kPa = 22.65 * exp(1.73 - 0.000157*h1); % Pressure (kPa)
P1 = P1_in_kPa * 1e3;                        % Pressure (Pa)

% Thermodynamic Flow properties
rho1 = P1 / (R * T1);                        % Density (kg/m^3)
a1 = sqrt(gamma * R * T1);                   % Speed of Sound (m/s)
V1 = M1 * a1;                                % Velocity (m/s)

% Wedge deflection angles (geometry)
theta1_deg = 7.64;                           % 1st wedge deflection (deg)
theta2_deg = 14.28;                          % 2nd wedge deflection (deg)

%% 1st Shock from Region 1 to Region 2
theta1 = theta1_deg * pi/180;                % Deflection angle (rad)

% Theta-Beta-Mach relation for Region 1
thetaBetaM1 = @(beta) atan( ...
   2 * (cos(beta)./sin(beta)) .* (M1^2 .* sin(beta).^2 - 1) ./ ...
   (M1^2 .* (gamma + cos(2*beta)) + 2) );

% Solve thetaBetaM1(beta1) = theta1 (weak shock solution)
beta1_in_deg = 36.85;                        % Calculated Beta (deg)
beta1_rad = beta1_in_deg * pi/180;           % (rad)
f1 = @(beta) thetaBetaM1(beta) - theta1;
beta1 = fzero(f1, beta1_rad);                % Shock Angle (rad)

% Normal Mach number Upstream
Mn1 = M1 * sin(beta1);
```

```
% Normal Shock relation (Region 1 to Region 2)
rho2_rho1 = ((gamma + 1)*Mn1^2) / (2 + (gamma - 1)*Mn1^2);
p2_p1 = 1 + (2*gamma/(gamma + 1))*(Mn1^2 - 1);
T2_T1 = p2_p1 / rho2_rho1;

% Normal Mach Downstream
Mn2_sq = (1 + 0.5*(gamma - 1)*Mn1^2) / ...
        (gamma*Mn1^2 - 0.5*(gamma - 1));
Mn2 = sqrt(Mn2_sq);

% Downstream Mach Number in Region 2
M2 = Mn2 / sin(beta1 - theta1);

% Region 2 static properties (Temperature, Pressure, and Density)
T2 = T1   * T2_T1;
P2 = P1   * p2_p1;
rho2 = rho1 * rho2_rho1;

% Region 2 Speed of Sound and Velocity
a2 = sqrt(gamma * R * T2);
V2 = M2 * a2;

%% 2nd Shock from Region 2 to Region 3
theta2 = theta2_deg * pi/180;               % Deflection angle (rad)

% Region 2 Upstream Values
M2_up = M2;
T2_up = T2;
P2_up = P2;
rho2_up = rho2;

% Theta-Beta-Mach relation for Region 2
thetaBetaM2 = @(beta) atan( ...
   2 * (cos(beta)./sin(beta)) .* (M2_up^2 .* sin(beta).^2 - 1) ./ ...
   (M2_up^2 .* (gamma + cos(2*beta)) + 2) );
f2 = @(beta) thetaBetaM2(beta) - theta2;
beta2_in_deg = 53.06;                       % Beta 2 (deg)
beta2_rad = beta2_in_deg * pi/180;          % (rad)
beta2 = fzero(f2, beta2_rad);               % Shock angle (rad)

% Normal Mach Upstream in Region 2
Mn2_up = M2_up * sin(beta2);

% Normal shock relation (Region 2 to Region 3)
rho3_rho2 = ((gamma + 1)*Mn2_up^2) / (2 + (gamma - 1)*Mn2_up^2);
p3_p2     = 1 + (2*gamma/(gamma + 1))*(Mn2_up^2 - 1);
T3_T2     = p3_p2 / rho3_rho2;

% Normal Mach Downstream from Region 2 to Region 3
Mn3_sq = (1 + 0.5*(gamma - 1)*Mn2_up^2) / ...
        (gamma*Mn2_up^2 - 0.5*(gamma - 1));
Mn3 = sqrt(Mn3_sq);

% Mach number in Region 3
```

```
M3 = Mn3 / sin(beta2 - theta2);

% Region 3 static properties (Temperature, Pressure, and Density)
T3   = T2_up   * T3_T2;
P3   = P2_up   * p3_p2;
rho3 = rho2_up * rho3_rho2;

% Region 3 speed of sound and velocity
a3 = sqrt(gamma * R * T3);
V3 = M3 * a3;

%% Dynamic Pressures in Region 1, Region 2, and Region 3
q1 = 0.5 * rho1 * V1^2;
q2 = 0.5 * rho2 * V2^2;
q3 = 0.5 * rho3 * V3^2;

%% Stagnation Pressure Ratios  in Region 1, Region 2, and Region 3
% Total Stagnation Pressures in each Region
P01 = P1 * (1 + (gamma - 1)/2 * M1^2)^(gamma/(gamma - 1));
P02 = P2 * (1 + (gamma - 1)/2 * M2^2)^(gamma/(gamma - 1));
P03 = P3 * (1 + (gamma - 1)/2 * M3^2)^(gamma/(gamma - 1));

% Ratios across each shock and cumulative
P02_P01 = P02 / P01;   % 1st shock (theta1)
P03_P02 = P03 / P02;   % 2nd shock (theta2)
P03_P01 = P03 / P01;   % cumulative

%% Printing Results
fprintf('Region 1 (Upstream Values at h = 50,000 ft / 15,240 m)\n');
fprintf('M1 = %.6f\n', M1);
fprintf('T1 = %.6f K\n', T1);
fprintf('P1 = %.6f Pa\n', P1);
fprintf('rho1 = %.6f kg/m^3\n', rho1);
fprintf('a1 = %.6f m/s\n', a1);
fprintf('V1 = %.6f m/s\n', V1);
fprintf('q1 = %.6f Pa\n\n', q1);
fprintf('Region 2 (Region 1 to Region 2 Downstream)\n');
fprintf('M2 = %.6f\n', M2);
fprintf('T2 = %.6f K\n', T2);
fprintf('P2 = %.6f Pa\n', P2);
fprintf('rho2 = %.6f kg/m^3\n', rho2);
fprintf('a2 = %.6f m/s\n', a2);
fprintf('V2 = %.6f m/s\n', V2);
fprintf('q2 = %.6f Pa\n\n', q2);
fprintf('Region 3 (Region 2 to Region 3 Downstream)\n');
fprintf('M3 = %.6f\n', M3);
fprintf('T3 = %.6f K\n', T3);
fprintf('P3 = %.6f Pa\n', P3);
fprintf('rho3 = %.6f kg/m^3\n', rho3);
fprintf('a3 = %.6f m/s\n', a3);
fprintf('V3 = %.6f m/s\n', V3);
fprintf('q3 = %.6f Pa\n', q3);
fprintf('\nStagnation Pressure Ratios\n');
fprintf('P02/P01 = %.6f\n', P02_P01);
fprintf('P03/P02 = %.6f\n', P03_P02);
```

```
fprintf('P03/P01 = %.6f\n\n', P03_P01);

%% Graphs with respect to position (Mach, Temperature, Static Pressure, Velocity,
Density, and Dynamic Pressure)
% Position along the nose and flow direction
x_start = -1;        % To see the upstream flow
x_end  = 3;          % choose as needed (3m)
Nx = 500;
x = linspace(x_start, x_end, Nx);

% Shock locations along x-Position
x_shock1 = 0.0;       % 1st shock at the nose
x_shock2 = 1.305;     % 2nd shock location (m) along the Edge

% Preallocate arrays for all properties vs x (Position)
M_x = zeros(size(x));   % Mach 1
T_x = zeros(size(x));   % Temperature 1 (K)
P_x = zeros(size(x));   % Pressure 1 (kPa)
rho_x = zeros(size(x)); % Density 1 (kg/m^3)
V_x = zeros(size(x));   % Velocity 1 (m/s)
q_x = zeros(size(x));   % dynamic pressure 1 (kPa)

% Indices for each region
idx1 = x <  x_shock1;                    % Region 1: Upstream of 1st Shock Wave
idx2 = x >= x_shock1 & x < x_shock2;     % Region 2: From 1st Shock to 2nd Shock
idx3 = x >= x_shock2;                    % Region 3: Downstream of 2nd shock

% Region 1 Upstream Values
M_x(idx1) = M1;
T_x(idx1) = T1;
P_x(idx1) = P1;
rho_x(idx1) = rho1;
V_x(idx1) = V1;
q_x(idx1) = q1;

% Region 2 Downstream of 1st Shock Values
M_x(idx2) = M2;
T_x(idx2) = T2;
P_x(idx2) = P2;
rho_x(idx2) = rho2;
V_x(idx2) = V2;
q_x(idx2) = q2;


% Region 3 Downstream of 2nd Shock Values
M_x(idx3) = M3;
T_x(idx3) = T3;
P_x(idx3) = P3;
rho_x(idx3) = rho3;
V_x(idx3) = V3;
q_x(idx3) = q3;

%% Plotting Sections
figure;
subplot(3,2,1);
```

```
plot(x, M_x, 'LineWidth', 2);
hold on;
xline(x_shock1, '--');
xline(x_shock2, '--');
grid on;
xlabel('x-position(m)');
ylabel('M');
title('Mach Number v. Position');
legend('M(x)', '1st Shock', '2nd Shock', 'Location', 'best');
subplot(3,2,2);
plot(x, T_x, 'LineWidth', 2);
hold on;
xline(x_shock1, '--');
xline(x_shock2, '--');
grid on;
xlabel('x-position(m)');
ylabel('T (K)');
title('Temperature v. Position');
legend('T(x)', 'Shock', 'Location', 'best');
subplot(3,2,3);
plot(x, P_x/1e3, 'LineWidth', 2);
hold on;
xline(x_shock1, '--');
xline(x_shock2, '--');
grid on;
xlabel('x-position(m)');
ylabel('P (kPa)');
title('Static Pressure v. Position');
legend('P(x)', 'Shock', 'Location', 'best');
subplot(3,2,4);
plot(x, V_x, 'LineWidth', 2);
hold on;
xline(x_shock1, '--');
xline(x_shock2, '--');
grid on;
xlabel('x-position(m)');
ylabel('V (m/s)');
title('Velocity v. Position');
legend('V(x)', 'Shock', 'Location', 'best');
subplot(3,2,5);
plot(x, rho_x, 'LineWidth', 2);
hold on;
xline(x_shock1, '--');
xline(x_shock2, '--');
grid on;
xlabel('x-position(m)');
ylabel('\rho (kg/m^3)');
title('Density v. Position');
legend('rho(x)', 'Shock', 'Location', 'best');
subplot(3,2,6);
plot(x, q_x/1e3, 'LineWidth', 2);
hold on;
xline(x_shock1, '--');
xline(x_shock2, '--');
grid on;
```

```
xlabel('x-position(m)');
ylabel('q (kPa)');
title('Dynamic Pressure v. Position');
legend('q(x)', 'Shock', 'Location', 'best');
```